KALMAN FILTER BASED FUSION OF CAMERA AND INERTIAL SENSOR
MEASUREMENTS FOR BODY STATE ESTIMATION

A THESIS SUBMITTED TO
THE GRADUATE SCHOOL OF NATURAL AND APPLIED SCIENCES
OF
MIDDLE EAST TECHNICAL UNIVERSITY

BY

GÖKÇEN ASLAN AYDEMİR

IN PARTIAL FULFILLMENT OF THE REQUIREMENTS
FOR
THE DEGREE OF MASTER OF SCIENCE
IN
ELECTRICAL AND ELECTRONICS ENGINEERING

SEPTEMBER 2009

Approval of the thesis:

KALMAN FILTER BASED FUSION OF CAMERA AND INERTIAL SENSOR MEASUREMENTS FOR BODY STATE ESTIMATION

submitted by **GÖKÇEN ASLAN AYDEMİR** in partial fulfillment of the requirements for the degree of **Master of Science in Electrical and Electronics Engineering Department, Middle East Technical University** by,

Prof. Dr. Canan Özgen   _____
Dean, **Graduate School of Natural and Applied Sciences, METU**

Prof. Dr. İsmet Erkmen   _____
Head of Department, **Electrical and Electronics Engineering, METU**

Assist. Prof. Dr. Afşar Saranlı   _____
Supervisor, **Electrical and Electronics Engineering, METU**

Examining Committee Members:

Prof. Dr. Kemal Leblebicioğlu   _____
Electrical and Electronics Engineering, METU

Assist. Prof. Dr. Afşar Saranlı   _____
Electrical and Electronics Engineering, METU

Prof. Dr. Engin Tuncer   _____
Electrical and Electronics Engineering, METU

Assist. Prof. Dr. Çağatay Candan   _____
Electrical and Electronics Engineering, METU

Dr. H. Burak Kaygısız   _____
Guidance and Control Division, TÜBİTAK-SAGE

Date: **September 11, 2009**

I hereby declare that all information in this document has been obtained and presented in accordance with academic rules and ethical conduct. I also declare that, as required by these rules and conduct, I have fully cited and referenced all material and results that are not original to this work.

Name, Last Name   :   Gökçen ASLAN AYDEMİR

Signature   :

ABSTRACT

KALMAN FILTER BASED FUSION OF CAMERA AND INERTIAL SENSOR MEASUREMENTS FOR BODY STATE ESTIMATION

Aslan Aydemir,Gökçen

M.S., Department of Electrical and Electronics Engineering

Supervisor : Assist. Prof. Dr. Afşar Saranlı

September 2009, 111 pages

The focus of the present thesis is on the joint use of cameras and inertial sensors, a recent area of active research. Within our scope, the performance of body state estimation is investigated with isolated inertial sensors, isolated cameras and finally with a fusion of two types of sensors within a Kalman Filtering framework. The study consists of both simulation and real hardware experiments. The body state estimation problem is restricted to a single axis rotation where we estimate turn angle and turn rate. This experimental setup provides a simple but effective means of assessing the benefits of the fusion process. Additionally, a sensitivity analysis is carried out in our simulation experiments to explore the sensitivity of the estimation performance to varying levels of calibration errors. It is shown by experiments that state estimation is more robust to calibration errors when the sensors are used jointly. For the fusion of sensors, the Indirect Kalman Filter is considered as well as the Direct Form Kalman Filter. This comparative study allows us to assess the contribution of an accurate system dynamical model to the final state estimates.

Our simulation and real hardware experiments effectively show that the fusion of the sensors eliminate the unbounded error growth characteristic of inertial sensors while final state estimation outperforms the use of cameras alone. Overall we can

demonstrate that the Kalman based fusion result in bounded error, high performance estimation of body state. The results are promising and suggest that these benefits can be extended to body state estimation for multiple degrees of freedom.

ÖZ

KALMAN FİLTRE İLE TÜMLEŞTİRİLEN ATALETSEL ÖLÇER VE KAMERA ÖLÇÜMLERİNDEN GÖVDE DURUM KESTİRİMİ

Aslan Aydemir, Gökçen

Yüksek Lisans, Elektrik ve Elektronik Mühendisliği Bölümü

Tez Yöneticisi : Yrd. Doç. Dr. Afşar Saranlı

Eylül 2009, 111 sayfa

Ataletsel ölçer ve kamera ölçümlerinin durum kestirimi amacı ile tümleştirilmesi son yıllarda aktif bir araştırma alanı haline gelmiştir. Bu tez çalışmasında tek başına ataletsel ölçerlerin, tek başına kameraların ve iki tür ölçerin bir arada kullanılmasının gövde durum kestirimi başarımına etkisi incelenmiştir. Ölçerler Kalman Filtre yapısı kullanılarak tümleştirilmiş, bilgisayar ortamında benzetimler ve laboratuar ortamında deneyler gerçekleştirilmiştir. Tek eksen etrafında dairesel hareket ile sınırlanan deneylerde dönme açısı ve dönme hızı tahmin edilmektedir. Kısıtlı tutulan hareket bu iki ölçerin tümleştirilmesinin kazandırdıkları konusunda açık bir değerlendirme ortamı sağlamaktadır. Çalışmada aynı zamanda kalibrasyon hatalarının kestirim başarımına etkisi benzetim ortamında incelenerek bir hassasiyet analizi yapılmıştır. İki ölçerin bir arada kullanılmasının hatalara karşı gürbüzlüğü arttırdığı gözlenmiştir. Tümleştirme Doğrudan Kalman Filtresi ile yapıldığı gibi Dolaylı Kalman Filtresi ile de gerçekleştirilmiştir. Böylece hassas bir dinamik sistem modelinin elde olmasının durum kestirimine etkisi değerlendirilmiştir.

Ataletsel ölçerlerden kaynaklanan hata artışının ölçerlerin bir arada kullanılması ile giderildiği ve bu tümleştirmenin tek başına kamera ile durum kestiriminden de daha

iyi sonuç verdiği benzetimlerde ve donanım ile yapılan deneylerde gözlenmiştir. Ataletsel ölçerler ve kameraların bir arada kullanılmasının zamanla artan hataları engellediği ve durum kestirimi hassasiyetini arttırdığı görülmektedir. Sonuçlar bu iki ölçerin bir arada kullanılmasının çok serbestlik dereceli sistemlerde de başarı olabileceğini düşündürmektedir.

Anahtar Kelimeler: Ataletsel Ölçer Birimi, Kamera Kalibrasyonu, Ataletsel Ölçer Birimi Kalibrasyonu, Ölçer Tümleştirmesi, Kalman Filtre

To my loving family

ACKNOWLEDGMENTS

TABLE OF CONTENTS

LIST OF TABLES

TABLES

LIST OF FIGURES

FIGURES

LIST OF SYMBOLS AND ABREVIATIONS

g frame   global (inertial) coordinate frame

b frame   body coordinate frame

c frame   camera coordinate frame

t frame   tangential coordinate frame

i frame   image coordinate frame

p frame   pixel coordinate frame

nom   nominal conditions

DI   Direct Integration

KF-G   Kalman Filter using only gyroscope (inertial) measurements

KF-C   Exteded Kalman Filter using only camera measurements

KF-GC   Extended Kalman Filter using gyroscope *and* camera measurements

IKF   Indirect Kalman Filter

MD   Mahalanobis Distance

$\mathbf{C_a^b}$ direction cosine matrix from general coordinate system *a* to *b*

x_p^a, y_p^a, z_p^a coordinates of point *p* in *frame a*

f   focal length of camera

(u_0, v_0)	image plane center, the center of projection
s_x	effective size of pixel in x direction
s_y	effective size of pixel in y direction
$\mathbf{K}_{int}$	internal camera matrix
$\mathbf{R}_{ext}$	external camera matrix (or the rotation matrix between the *c-frame* and *g-frame*)
P	3D point observed by the camera in the scene
r	radius of rotation
w	angular (rotational) velocity input
ω	actual angular velocity of the rate table
θ	actual angular position of the rate table
a_t, a_c	tangential and centripetal acceleration
V_t	tangential velocity
$\mathbf{F(k)}$	state transition matrix
$\mathbf{G(k)}$	control-input matrix
$\mathbf{H(k)}$	measurement(observation) matrix
$\mathbf{Q(k)}$	process noise covariance matrix
$\mathbf{R(k)}$	measurement noise covariance matrix
$\mathbf{J(k)}$	Jacobian Matrix of measurement function

CHAPTER 1

INTRODUCTION

Navigation is formally defined as the process of directing a vehicle in order to reach the intended destination [1]. Several techniques have been used throughout history including the well-known *north following* by using a compass and observing the North Star (for northern hemisphere). Although they are still used, these techniques have largely been replaced by the use of electronic sensors for most applications.

It is possible to navigate with the assistance of sensors such as inertial sensors, radars, odometers and satellite global position systems as well as electronic information sources such as digital maps and sky atlases. Which particular sensor and data is suitable largely depends on the specific platform and application. However, the development of inertial sensors made them indispensable for the navigation of mobile platforms. They are reliable sensors in the sense that they cannot be affected from outside with natural and man-made disturbance sources. Whether the platform is a ship, an airplane, a land vehicle or a person, the output of inertial sensors is determined by the motion of the body through Newton's Laws of Motion and planetary physics.

Inertial sensors consist of *accelerometers* and *gyroscopes* which measure the body acceleration and the angular turn rate respectively along their corresponding axes of measurement. A complete 6 *degree-of-freedom* (DOF) measurement set-up is obtained by combining 3 orthogonal accelerometers with 3 orthogonal gyroscopes in a package called the *Inertial Measurement Unit* (IMU). The outputs of the inertial sensor can be used to measure a number of physical variables associated with the

1

motion of the moving platform. In particular, with the knowledge of initial position, velocity and orientation, these three variables (also known as the *navigation variables*) can be tracked by integrating the output of the IMU at each time step. This procedure is called dead-reckoning (DR). As new manufacturing technologies for these sensors such as *Micro Electro-Mechanical Systems* (MEMS) technology result in the price drop for these sensors, the application areas are rapidly growing and the sensors are becoming of interest for a wider range of applications including for example many non-military applications. Examples include automotive applications for collision detection and advanced tire slip and sliding control[2]; mobile robotics including automated ground vehicles [3],[4],[5],[6], aerial vehicles [7],[8] and even consumer electronics for personal applications [9].

However, the use of inertial sensors suffers from bias errors which accumulate in time through the calculation of output variables. One idea from the literature is the use of multiple sensors with possibly complementing characteristics to obtain a fusion performance that is better than any individual sensor. To overcome the accumulation of errors with inertial sensors, inertial sensors are mostly used in combination with Global Positioning Systems (GPS) since GPS supplies error bounded (absolute) measurements. However, GPS data has low accuracy. Other problems include the much smaller sampling rate of the GPS data as compared with an IMU as well as the fact that GPS beacon signals originate outside of the moving platform and hence prone to service failure or external disturbances, intentional or otherwise.

Research on using visual sensors instead as complementary devices to IMUs and Inertial Navigation Systems (INS) has been increasing since the beginnings of 2000s. Given a fixed visual landmark, Cameras can provide bounded error (absolute) measurements of certain motion variables as opposed to IMUs. For example, a stereo camera pair can provide bounded error position information with respect to a known landmark by triangulation. Known spatial relationships between multiple visual

landmarks can be used even by a single camera to provide similar position information. Yet, the raw camera output is a two dimensional image array which requires intensive processing time and the camera sampling rate (e.g. 30 frames per second) is therefore much smaller than that of an IMU (often several samples per second).

However, even with these limitations, a camera can complement an IMU in such a way that the fusion of the two sensors can outperform both the IMU alone as well as the camera alone. The focus of this thesis is to make and investigate this claim by providing simulation based as well as hardware based experiments conducted in a controlled experimental setup.

1.1 Previous Work

The idea of combining visual and inertial sensors materialized in late 1990's and has been developing since then. There are examples of the combined usage of IMU and a camera in the literature. This combination has been used for navigation [10], object shape recovery [11],[12] and augmented reality applications[13],[14]. A solid understanding of the characteristics and calibration of inertial sensors and cameras as well as of the processing steps for the sensor data is an important task on the way to successful sensor fusion. Inertial sensor basics and strapdown inertial navigation systems are described in detail by Titterton and Weston [15]. Information about MEMS technology and MEMS inertial measurement is included in this second edition of the book. Inertial navigation system aiding including GPS, radars, barometers, terrain maps are explained describing the system integration methodology and application areas. The book considers only the military applications of visual aiding. Continuous Visual Navigation (CVN) is explained which compares extracted linear features from aerial images of the terrain with the database images.

Trucco and Verri [16] provide a good reference text for understanding the basics and the key points of vision topics including 3D camera geometry. Cameras are mostly represented with a pinhole camera model which simplifies the camera lens to its ideal behavior. Camera calibration is necessary to relate information obtained from the image plane pixels to objects in the real world. There has been extensive research carried out on camera calibration techniques most of which are developed by the *computer vision* (CV) community. The most well-known techniques for single and multiple camera calibration were presented by Tsai [16], Heikkilä and Silven [18] and Zhang [19].

The method by Tsai assumes that some of the parameters are known initially. These include parameters supplied by the manufacturer of the camera. The center of projection which is assumed to be in the middle of the image is not estimated by this algorithm. A set of linear equations are solved which are formed by using the radial alignment constraint using a 3D or 2D calibration grid.

Heikkilä & Silven present a four step camera calibration technique by first introducing a closed-form solution using a direct linear transform (DLT) which assumes a simpler pinhole camera model to initialize the camera parameters. At the second step, a non-linear estimation process is carried out by employing Levenberg-Marquardt algorithm where distortion parameters are included in the camera model. The next two steps handle the problems of image correction and problems caused by illumination. The final estimated parameters include radial and decentering distortion as well as the main outputs which are the internal and external calibration parameters.

Zhang uses the snapshots of a checkerboard pattern taken at different orientations where the corners are extracted to compute projective transformations. Closed form solution is computed analytically which is followed by a non-linear refinement based

on maximum likelihood. The model used in Zhang's method contains radial distortion terms up to fifth order.

Camera calibration extensively studied with many more techniques presented in the literature. These are out of the scope of this thesis and here, we make use of the *camera calibration toolbox* developed by Jean-Yves Bouguet at the Vision Laboratory of California Institute of Technology [20] for internal and external calibration. The model employed in this toolbox is similar to the model used by Heikkilä & Silven mentioned in previous paragraphs. The process is described in Section 2.2.3.

Calibration between inertial measurement units and cameras is composed of determining the relative geometrical layout of the IMU axes set and the camera image plane. This is also an active research area. IMUs and cameras were first used together on aerial applications hence calibration methods using aerial images were developed for this purpose. This method is still active as new research is being carried out [21]. In this particular method, the geometric relationship between the IMU and camera is extracted considering the IMU measurements and aerial images of a land piece marked in squares. However, this method is expensive, time consuming and is not feasible for cameras with smaller field of view. Research on joint camera-IMU calibration yielded two different methods which are accepted by the robotics community. Lobo studied finding the orientation between the IMU axes and camera axes by observing a perfectly vertical black and white checkerboard pattern [22], [23]. Images and accelerometer readings are collected for several positions of IMU-camera assembly with the assumption that gyroscope axes are aligned with accelerometer axes or that any misalignment has been previously corrected. Parallel checkerboard lines are no more parallel in the image and they intersect somewhere in or outside the image. The intersection point is called the vanishing point and the normal to the plane defined by the converging lines is a direction of the gravity vector. Making a comparison between the components of the

5

gravitational acceleration on each accelerometer axis, Euler angles between the IMU and the camera are calculated. A toolbox InerVis [24] written for MATLAB to perform these steps. This toolbox is also compatible with the Camera Calibration Toolbox for computing camera internal calibration parameters.

A more recent study on the same subject addresses the *Error State Kalman Filter* under the Extended Kalman Filtering frame-work. Error State EKF estimates the error on the tracked variables instead of the variables themselves. The proposed algorithm is an extension to 6 DOF body state error estimation using inertial and visual sensor measurements. The translation vector and rotation matrix between the coordinate systems of the sensors are added to the state variables resulting in an augmented state vector. This augmented state vector is then estimated by observing a checkerboard pattern. It is shown that the state vector converges to the true state and calibration while the covariance matrix indicates decreasing estimation variance [25]. This work is important in the sense that calibration and state estimation are combined in one filter without the need for an accurate model of platform dynamics. This is an advantage of the Error State Extended Kalman Filter. This method was studied by Roumeliotis et.al with a simplified 2D example [26].

J.Blomster also studied with Extended Kalman Filter for combining camera and gyroscope measurements for orientation estimation [27]. Rotation is estimated based on the lines in the image which are extracted with Canny edge detector. Klein and Drummond also use edge detectors in their algorithm for visual tracking [28]. Motion blurs caused by fast motion are also estimated and corrected in this tightly-integrated algorithm (Figure 1).
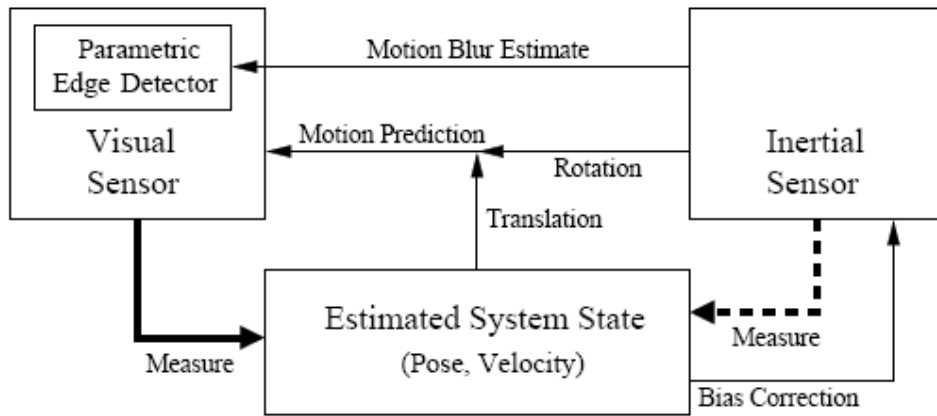
Figure 1 – Tightly integrated sensor fusion strategy of Klein&Drummond [28].

Finally, Strelow prefers using an Iterated Extended Kalman Filter structure for combining inertial and visual measurements in his PhD dissertation thesis [29]. This study includes a comprehensive survey on motion estimation and robust visual tracking. Strelow also discusses the short-term and long-term effects of sensor errors to estimation performance.

1.2   Scope and Contribution

This thesis study is intended to develop an algorithm to combine the measurements of inertial and visual sensors for body state estimation. The main motivation of this research is to acquire the background knowledge of this attractive subject and implement a general fusion algorithm that is tested in a simplified system with the help of simulation and real hardware experiments. Although the experiments are carried out with a single degree-of-freedom (rotational motion) system, we believe this simplified setup preserves the general characteristics of the problem while

making its mathematical and experimental study much more accessible. We believe the conclusions of the thesis can be readily extended to six degree-of-freedom case.

The main objective of this study is achieved by implementing an Extended Kalman Filter considering the dynamical model of moving body (a motion controlled rate-table) which is a part of the real experimental set-up. Body state estimation was carried out by using sensors individually and jointly within the considered fusion framework. The thesis results experimentally demonstrate that using sensors jointly yields a more robust and better performing body state estimator. This conclusion, which is first suggested by simulation experiments, is then later verified with real hardware experiments.

Another contribution of the thesis is a comparison of the performance of Indirect Kalman Filter with a Direct Extended Kalman Filter on the same problem. Indirect (or Error State) Kalman Filters have also been extensively studied in the literature within the navigation systems research community and represent a different approach to the body state estimation problem. The mathematical formulations for both approaches were considered in some text books with the statement of advantages and disadvantages for each. However in this work we present a comparison considering the experimental results. Since the Indirect Kalman Filter does not use moving body dynamic model, this comparison in which the Direct form outperforms the Indirect form, illustrates the gains in estimation performance by the use of an accurate system dynamic model. Other advantages and disadvantages are also discussed. Finally, the thesis contributes by a simulation experimental sensitivity analysis with respect to system calibration parameters where the performance of the Extended Kalman Filter is studied under controlled disturbances to the calibration parameters.

1.3   Outline of the Thesis

We have begun in this chapter by presenting information on recent research on inertial sensor - camera fusion and joint IMU-camera calibration as well as the scope and contribution of the study. Chapter 2 contains background on sensor technology, sensor models, sensor calibration techniques and procedures in particular for IMUs and Cameras. Kalman Filtering framework is reviewed in Chapter 3 focusing on Kalman, Extended Kalman and Indirect (Error State) Kalman Filters. The State-space formulation of the dynamical system which is our moving platform is presented in Chapter 4 where we also define the various coordinate systems that are used in modeling and calibration of the system. The thesis continues then by presenting first the simulation experiments in Chapter 5 and then the real hardware experiments in Chapter 6, covering both methodology and experimental results. The comparison of Kalman, Extended Kalman and Indirect (Error State) Kalman performances are also presented within the scope of these chapters. Finally Chapter 7 summarizes our conclusions for the thesis and discusses possible future directions.

CHAPTER 2

BACKGROUND ON SENSORS AND CALIBRATION

We begin in this Chapter by presenting characteristics and mathematical models as well as the calibration procedures of the two sensor types that we consider for the thesis: the IMU and the Camera. These steps are indispensable and integral part of the work that is presented in the thesis and hence merits attention. We begin by considering IMUs, and then we move on to cameras.

2.1 Inertial Sensors

IMUs are combination sensors which can measure translational (accelerometers) and rotational motion (rate gyroscopes) that a moving sensor body experiences. This is done by means of different technological approaches that are outlined briefly.

2.1.1 Inertial Sensor Technology

Current IMU technology offers the user to make a choice between different types of sensors depending on the application. It is possible to find pendulous, vibrating or MEMS (Micro Electro- Mechanical Systems) accelerometers but we are not interested in accelerometers for this particular work.

The first gyroscope is a mechanical one consisting of a spinning wheel or rotor. In case of rotation, the gimbals turn but the rotor points the same direction despite this rotation due to the principle of preservation of angular momentum. Gimbaled

mechanical gyroscopes are still in use and they provide accurate information with today's metal treatment technology. However, this technology is expensive and mechanical gyroscopes are large in size. As a result, small, light weight and less expensive sensors are in use in many inertial navigation systems (INS). In addition, these systems do not suffer from mechanical complexities. The sensor unit is rigidly attached to the rotating body which is called a *strapdown system* experiencing the same motion with the body.

In modern systems, several types of gyroscopes are employed:

- Vibratory gyroscopes
- Nuclear magnetic resonance(NMR) gyroscopes
- Electrostatic gyroscopes(ESG)
- Ring laser gyroscopes(RLG)
- Fiber optic gyroscopes(FOG)
- MEMS gyroscopes

The usage of RLG's and FOG's are wide spread, especially in military applications considering their accuracy. MEMS sensors can be preferable considering their extremely small size, economic power consumption and their cheap price if the accuracy expectation is low. Because, they are still not accurate enough and they are sensitive to noise. But every day new MEMS IMUs are introduced to the market with lower noise levels.

The drawbacks of using strapdown IMUs are that they require computational complexity and they suffer from errors growing with time. The error sources will be mentioned in next section.

2.1.2 Inertial Measurement Unit Errors

Both accelerometers and gyroscopes suffer from measurement errors. It is critical to know the behavior of a sensor to make meaningful use of the sensor measurements.

11

Characterizing sensor errors is also an essential task for simulating sensor measurements. Sensor errors are collectively represented by a mathematical model which is also used for calibrating the sensor. This model is often utilized in navigation algorithms to obtain accurate estimates of final variables of interest such as body velocity, position and Euler angles. These variables are often called the *navigation outputs.*

Main types of error are similar for accelerometers and gyroscopes. *Fixed bias error* is observed in many sensors as well as accelerometers and gyroscopes. It is defined as the sensor output even in the absence of an applied physical input. This term is called *drift* or *g-independent bias* in the case of gyroscopes. *Scale factor error* is the ratio of output change to the input change causing that output. Misalignments in orthogonality between the axis of sensor triads cause *cross-coupling errors.* In addition, gyroscopes experience *g-dependent bias errors* which are proportional to the applied acceleration. Apart from the mentioned error sources, mathematical sensor models might be extended with higher order terms [15]. However, they are out of the scope of this thesis.

Equations (1) and (2) characterize the error models for the accelerometer and the gyroscope triads where δf and $\delta \omega$ stand for the accelerometer and gyroscope measurement errors respectively.

$$\begin{bmatrix} \delta f_x \\ \delta f_y \\ \delta f_z \end{bmatrix} = \mathbf{B_A} + \mathbf{S_A} \begin{bmatrix} \alpha_x \\ \alpha_y \\ \alpha_z \end{bmatrix} + \mathbf{M_A} \begin{bmatrix} \alpha_x \\ \alpha_y \\ \alpha_z \end{bmatrix} + w_A \tag{1}$$

$$\begin{bmatrix} \delta \omega_x \\ \delta \omega_y \\ \delta \omega_z \end{bmatrix} = \mathbf{B_G} + \mathbf{B_g} \begin{bmatrix} \alpha_x \\ \alpha_y \\ \alpha_z \end{bmatrix} + \mathbf{S_G} \begin{bmatrix} \omega_x \\ \omega_y \\ \omega_z \end{bmatrix} + \mathbf{M_G} \begin{bmatrix} \omega_x \\ \omega_y \\ \omega_z \end{bmatrix} + w_G \tag{2}$$

Here, α_x, α_y, α_z represent the actual accelerations and ω_x, ω_y, ω_z represent the angular rates that are applied on each axis. $\mathbf{B_A}$ and $\mathbf{B_G}$ are 3x1 vectors consisting of the bias elements on each axis. $\mathbf{S_A}$ and $\mathbf{S_G}$ are diagonal 3x3 matrices whose elements represent the scale factor for each axis. There may be scalar terms if all axes have identical scale factors. $\mathbf{M_A}$ and $\mathbf{M_G}$ are the orthogonality matrices composed of cross coupling error coefficients. Matrix $\mathbf{B_g}$ contains the g-dependent bias coefficients for the gyros. Finally, w_A and w_G are the noise terms which are usually assumed white Gaussian[30]. The sensor measurements can be represented with the summation of the actual accelerations/angular rates with the sensor errors $\boldsymbol{\delta f}$ and $\boldsymbol{\delta \omega}$. It may be useful to state that the sensor errors are modeled in terms of the true accelerations and angular rates since this formulation is useful in Kalman Filtering framework especially for Indirect Kalman Filter applications.

The general error models given above are also valid for the considered MEMS IMU. Indeed, $\mathbf{M_A}$ and $\mathbf{M_G}$ matrices play a more important role since the raw measurements do not represent an orthogonal right handed coordinate system. To obtain such measurements, the raw data should be multiplied with these matrices.

Static (no-motion) and quasi-static (step motion) experiments are conducted for the characterization of our sensor. During static tests, data is collected while the sensor is at rest at various configurations. The aim is to calculate some of the calibration parameters. The procedures and results of these tests are given separately for accelerometers and gyroscopes in the following sections.

2.1.3 IMU Calibration

In this work MicroStrain 3DM-GX1 MEMS IMU is   package is subjected to several tests in order to determine the calibration parameters mentioned in section 2.1.2.

3DM-GX1 contains 3 MEMS accelerometers, 3 MEMS gyroscopes and 3 magnetometers. Magnetometers measure the body axis components of the Earth's magnetic field, however, in the present study, magnetic field measurements are not used. The sensor assembly is capable of communication via RS232 serial port. The user may write a program to get the sensor outputs or may use the graphical user interface of the sensor. It is possible to request raw sensor measurements as well as the sensor outputs converted to physical units with internal calibration routines. A microprocessor is present inside the sensor package to supply stabilized Euler angles by running integration algorithms. However, in order to have complete control on sensor measurements, raw measurements are collected from the IMU in this study. The calibration parameters are determined throughout the following tests and the raw measurements are converted to physical units [31].

2.1.3.1 Accelerometer Characterization

- *Multi-Position Static Tests*

Multi-position static tests are done with the purpose of determining the *static bias*, *scale factor* and *scale factor non-linearity*. Accelerometers are mounted on an index table (Figure 2) capable of measurable (manual) axis rotation with a resolution of 1 degree. The table is rotated so that the measured gravitational acceleration is known due to a known angle with the absolute vertical and will vary between 1g and -1g. Two controlled rotary axes of the table apply this gravitational acceleration variation to the y-axis and z-axis of the sensor case respectively. Hence, we can measure the decomposition of the gravitational acceleration vector along the corresponding sensor measurement channels. The step size for the test is determined to be 30º resulting in 12 measurement positions for a 360 degree full turn. Approximately 60 seconds (about 6000 samples) data is recorded for each step to compensate for

random noise. We observe a sinusoidal pattern as expected due to the trigonometric functions involved in this decomposition.

- *Bias calculation*

Raw sensor outputs collected from raw channels C1 and C2 of 3DM-GX1 are given in Figure 3. Raw data is the raw voltage output coding form the sensor A/D converter where 0 represents 0 volts and 65535 represent 5 volts. Again note that raw channels are not necessarily orthogonal to each other. However for this particular sensor, C1, C2 and C3 mostly correspond to the z, y and x-axis on the orthogonal case frame. The raw sensor outputs (Figure 3) are compared with the sensor input (determined by the index table setting) and scaled to physical units after calculating bias and scale factor values.

Figure 2- Index table with 3DM-GX1 shown on top (330 degrees orientation around the sensor y-axis)

Raw data recorded at each step is noisy as shown in Figure 3. Mean value of each step is calculated before calculating the bias value. The mean value of the new stepwise waveform should be zero. Hence, the mean value of the stepwise waveform for a particular channel corresponds to the bias value of that channel. Bias values

channel C1, C2 and C3 are obtained as 32846.3, 32627.7 and 32989 respectively which match exactly with the manufacturer provided calibration sheet values.
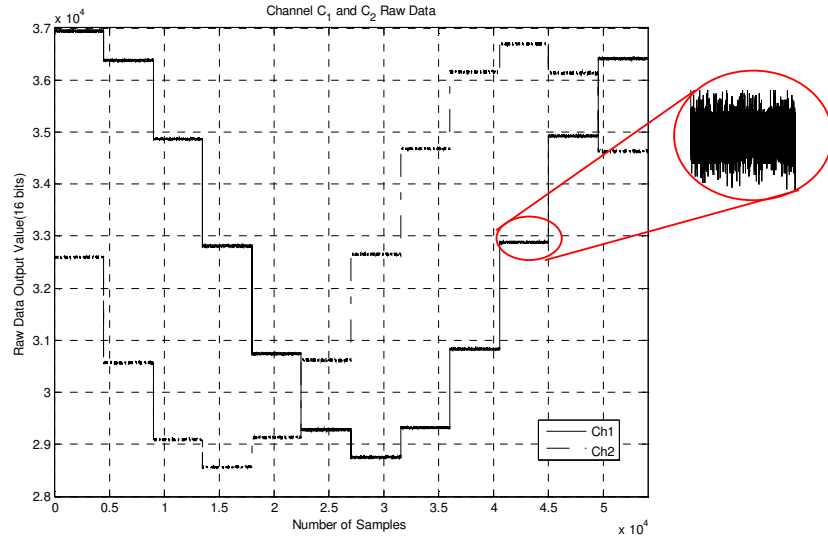
Figure 3- C1 and C2 raw outputs. The figure x-axis corresponds to readings from the sensor and since the index table rotation is done manually approximately every 60 seconds, each level is not exactly of equal duration.

- *Scale factor calculation*

Scale factor calculation is one of the main steps to obtain the physical quantities form the raw sensor outputs. The known input and the recorded sensor output are compared after the raw sensor data is compensated for the bias value. The ratio of the bias compensated output and the input is the scale factor. The input and the calibrated output of the sensor for Ch.1 are shown in Figure 4 below. The mean values of 12 data sets are computed and compared with inputs at 12 different positions.

16
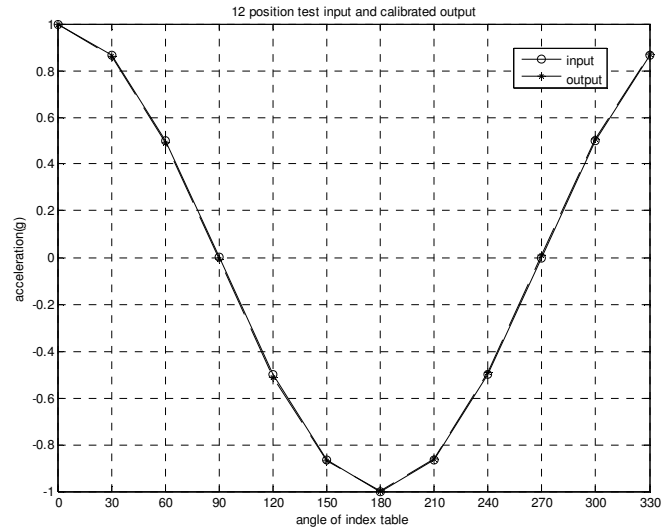
Figure 4 - Relationship between Channel C1 input and the calibrated output.

- *Scale factor nonlinearity*

Scale factor is calculated as the ratio of input to sensor output as explained in previous paragraph. Scale factor may have slightly different values when the accelerometer is subject to clockwise and anti-clockwise rotation in the gravity plane. This nonlinearity is not observed of the accelerometers in use.

- *Cross-coupling coefficients*

Misalignment between the triaxial sensor configuration can be found by solving Eqn(3) after collecting data from the sensor at different axes orientations. Scale factor for each sensor is calculated in previous section after levelling the sensors to elliminate the cross-coupling effect. For calculation of this effect, the IMU case is mounted such that true accelerometers [α_x, α_y, α_z] will be [1g,0g,0g], [0g,1g,0g] and [0g,0g,1g]. Scale factor coefficients, bias coefficients and the actual accelerations and acceleration measurements for each orientation are known. Having only the

17

misalignment coefficients unknown, misalignment coefficients are obtained by solving Eqn.(3).

$$\begin{bmatrix} \tilde{\alpha}_x \\ \tilde{\alpha}_y \\ \tilde{\alpha}_z \end{bmatrix} = \begin{bmatrix} S_{Ax} & 0 & 0 \\ 0 & S_{Ay} & 0 \\ 0 & 0 & S_{az} \end{bmatrix} + \begin{bmatrix} 1 & m_{xy} & m_{xz} \\ m_{yx} & 1 & m_{yz} \\ m_{zx} & m_{zy} & 1 \end{bmatrix} \begin{bmatrix} \alpha_x \\ \alpha_y \\ \alpha_z \end{bmatrix} + \begin{bmatrix} B_{Ax} \\ B_{Ay} \\ B_{Az} \end{bmatrix} \quad (3)$$

- *Single Position Static Tests*

Data from stationary accelerometers are collected for several hours to observe the statistical properties, i.e. *mean* and *standard deviation* of the sensor random noise on the outputs and effect of internal temperature change on the sensor outputs.

- *Analyzing Thermal Characteristics*

The performance of MEMS sensors with changing temperature has been studied and it is claimed that a warm-up period is needed for the output to stabilize [30]. In standard IMU calibration, thermal tests are carried out in thermal chambers with carefully controlled internal temperature. Since we did not have this capability, a warm-up test in ambient temperature (25ºC) is conducted. The internal temperature of 3DM-GX1 is observed for 6 hours including its warm-up period where sensor internal temperature increases from ambient to operating value (Figure 5). Data from accelerometers and internal thermometer is collected. Contrary to the observation in [30], no change is observed in output mean values for this sensor (Figure 6). Sensor output data is shown with the moving averaged filter output. Although not specified by the manufacturer, there may be a temperature compensation algorithm within the sensor processor. Therefore, a thermal error model within this range of temperatures (22ºC to 38ºC) is not recommended. Note however that the there may still be a

18

temperature dependence when the sensor is subjected to higher temperatures. However that the there may still be a temperature dependence when the sensor is subjected to higher temperatures.
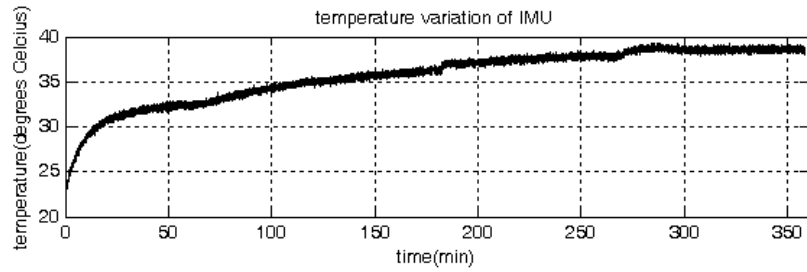
Figure 5- Internal temperature profile (ºC) for 6 hours of MicroStrain 3DM-GX1.
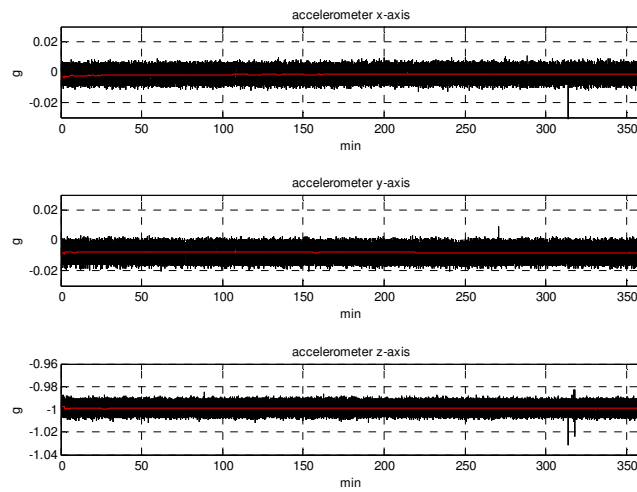
Figure 6- Accelerometer thermal test data. Outputs are recorded for 6 hours. Data after filtering with a moving average filter is shown in red.

19

- *Noise Characteristics*

Ideally, due to the gravitational acceleration, constant outputs are to be observed on all output channels. (Note from the above model that no single channel output may necessarily coincide exclusively with the gravitational axis). In practice, a noisy characteristic is observed as expected. The standard deviation of the noisy measurements determines the characteristics of white Gaussian noise, w_A. After the raw measurements are converted to physical units, standard deviation of w_A is found to be 0.0024g, 0.0026g and 0.0031g for x,y and z axis respectively.

- *Bias instability*

A simple measure of bias is the average of the long term sensor data. *Bias stability* is an important parameter in the calibration and performance classification of accelerometers and represents the changes in bias with time. Allan-variance (AVAR) method [33] developed for analyzing the instability of GPS clock measurements is also used for inertial sensor bias instability calculations traditionally. AVAR is based on analyzing the expected value of the data by partitioning the data sequence into bins with gradually increasing number of samples by considering an *averaging time* parameter τ. Allan Variance expression is given in(4).

$$\sigma^2(\tau) = \frac{1}{2(n-1)} \sum_i \left(y(\tau)_{i+1} - y(\tau)_i \right)^2 \qquad (4)$$

Collected data is divided into bins of averaging time τ and the data in each bin is averaged where $y(\tau)_i$ represents the average of bin i and n is the total number of bins. *Allan Deviation*, $\sigma(\tau)$ is the square root of Allan Variance. Allan Deviation graph for z-axis accelerometer is plotted in Figure 7 as a function of averaging time τ. The minimum point on the graph is considered to be the best possible bias instability.
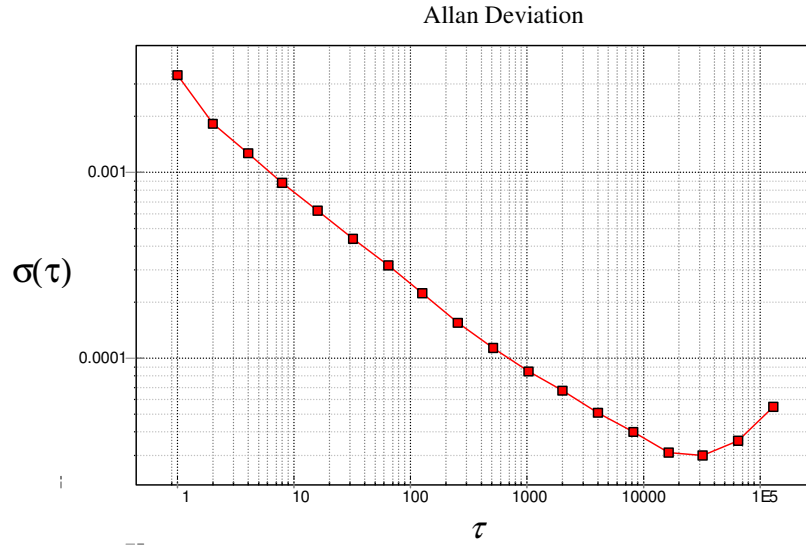
Figure 7- The Allan-Variance curve for the static bias for the z-axis.

Bias instability indicates the change in fixed bias value. Instead of using a fixed bias assumption for sensors, bias value is estimated by assuming fluctuations on the order of calculated bias instability around the fixed bias value For the considered IMU accelerometers, a bias stability of 130μg, 100μg and 43μg are obtained for orthogonalized x, y and z axes respectively.

Gyroscope Tests

- *Rate Transfer Tests*

The purpose of rate transfer tests is to analyze the characteristics of the scale factor, i.e., to analyse the relationship between the change in the input turn rate and the sensor output data as a controlled stepping motion is applied to the sensor. This is realized on a rotating table called *the rate table* [34]. The rate table receives angular acceleration, angular velocity and angular position commands from RS232 port through its graphical interface.

21
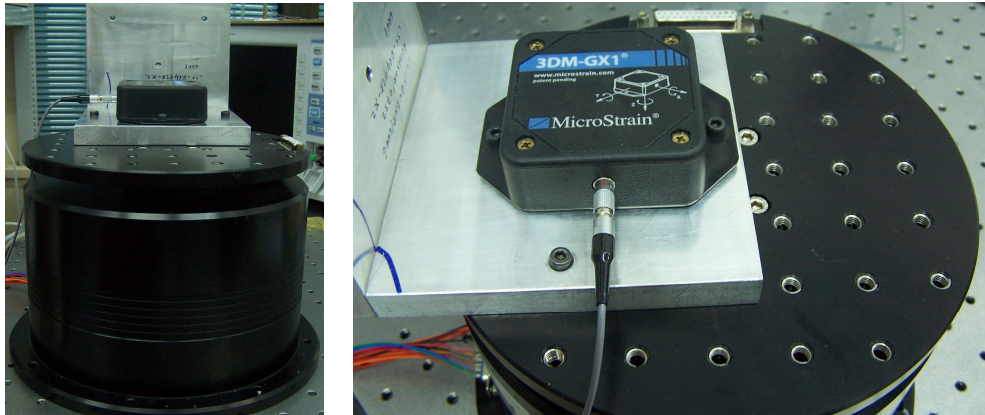
Figure 8 – MicroStrain 3DM-GX1 mounted on IMAR Rate Table with a mechanical interface.
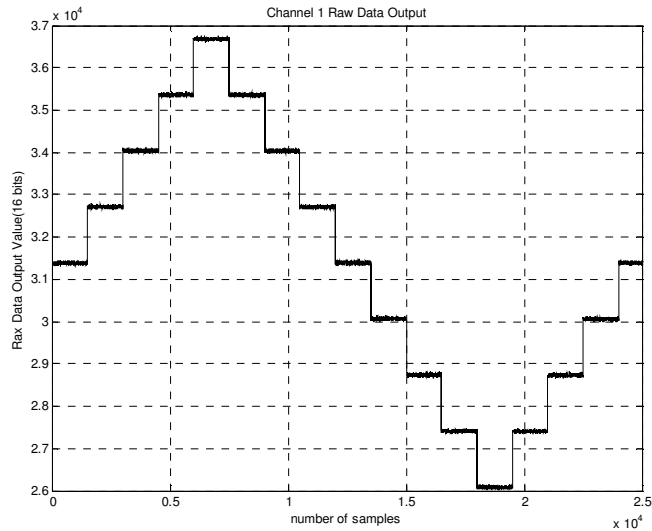
Figure 9- Gyroscope C1 raw output data as response to a stepwise constant turn rate on the rate table

3DM-GX1 is placed on the rate table via a mechanical interface as shown in Figure 8. The rotation rate of the rate table is increased in a stepwise manner starting from zero and varying between desired maximum and minimum rates [15] as illustrated in Figure 9. Step size and maximum rate are chosen to be 20º/sec and 80º/sec respectively. Gyroscope data is recorded at each step and the output is compared

with the input to obtain the scale factor and bias value as well as to observe any existing nonlinearity.

- *Drift calculation*

Gyroscope drift calculation is similar to accelerometer bias calculation. The stepwise rate test output is averaged and numerical drift values for channels C1, C2 and C3 are obtained to be 31385, 31190 and 33618 respectively.

- *Scale factor and scale factor nonlinearity*

Scale factor of each channel is calculated by finding the ratio of the drift-compensated output to the angular rate input. With the aim of observing the nonlinearity on the scale factor, the input-output relationship is analyzed for clockwise and anti-clockwise rotation. Note that the input-output relationship is linear and there is no hysteresis effect (Figure 10). This indicates that the scale factor is a constant and does not depend on the direction of rotation.
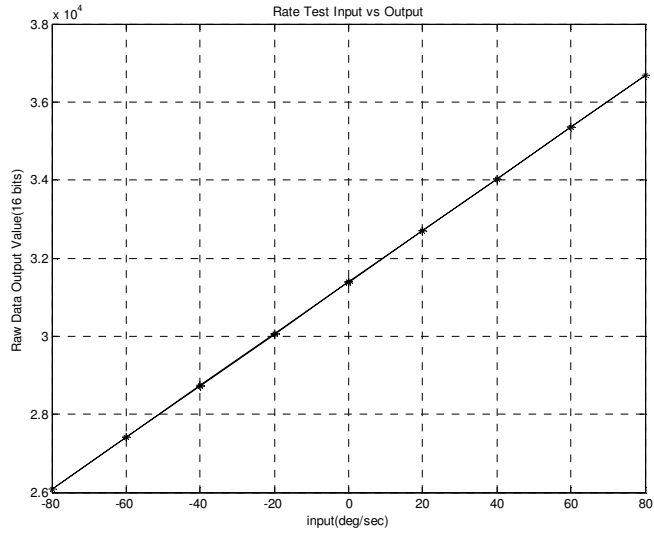
Figure 10 – Drift compensated gyroscope output versus the controlled input turn-rate. The linear relation is represented by a scale factor. The slope of the curve is constant for clockwise and counter-clockwise rotation indicating the absence of scale-factor nonlinearity.
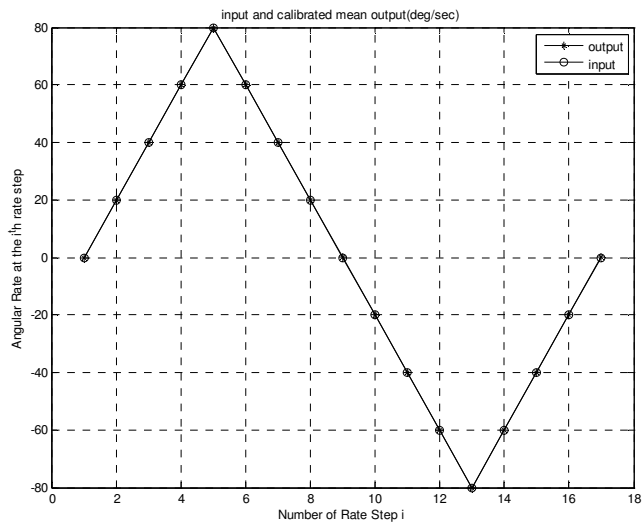
Figure 11- Channel 1 input and calibrated output. Rotation rate varies between +80º/sec and -80º/sec with 20º/sec steps.

24

After obtaining drift and scale factor values, raw measurements were converted to physical units. In Figure 11, , the plots of input and output rates are drawn with respect to rotation rate step number and given together in units of degrees/second in y axis. Note that, the mean value of each noisy data set for each step is used in this figure.

- *Multi Position Dynamic Test*

Gyroscope bias coefficients and misalignment errors can be determined through multi position dynamical tests. For accelerometers, we use the gravity as the reference input and calculate the model coefficients by comparing the input with the output. In the case of gyroscopes, it is possible to obtain the model parameters by rotating IMU with known angular input rate. The orientation of the IMU is changed to change the gyroscope measuring the rotation. Collecting test data with different orientations, Eqn.(5) is solved and the coefficients are determined.

$$
\begin{bmatrix} \tilde{\omega}_x \\ \tilde{\omega}_y \\ \tilde{\omega}_z \end{bmatrix} = \begin{bmatrix} S_{gx} & 0 & 0 \\ 0 & S_{gy} & 0 \\ 0 & 0 & S_{gz} \end{bmatrix} + \begin{bmatrix} 1 & m_{xy} & m_{xz} \\ m_{yx} & 1 & m_{yz} \\ m_{zx} & m_{zy} & 1 \end{bmatrix} \begin{bmatrix} \omega_x \\ \omega_y \\ \omega_z \end{bmatrix} + \begin{bmatrix} B_{gx} \\ B_{gy} \\ B_{gz} \end{bmatrix} + \begin{bmatrix} B_{ga_{xx}} & B_{ga_{xy}} & B_{ga_{xz}} \\ B_{ga_{yx}} & B_{ga_{yy}} & B_{ga_{yz}} \\ B_{ga_{zx}} & B_{ga_{zy}} & B_{ga_{zz}} \end{bmatrix} \begin{bmatrix} a_x \\ a_y \\ a_z \end{bmatrix} \quad (5)
$$

Traditionally, the above coefficients are calculated by taking the earth rotation rate as the reference input and collecting gyroscope data when the sensor is stationary[15]. However, this procedure requires precisely positioning the sensor assembly measurement axes with the north-east-down frame [15]. It is necessary to determine the north before collecting data. This method is still widely used in tactical or navigation grade IMU's where the sensors are more sensitive. On the other hand, the higher noise of MEMS IMUs could overshadow the earth rotation rate components on the axis. For this reason, the abovementioned technique is proposed, with an input overcoming the earth rotation rate.

- *Single Position Static Test*

3DM-GX1 is capable of supplying accelerometer and gyroscope data concurrently. During the single position static tests described previously for accelerometers, outputs of all sensors are captured. Noise and thermal characteristics of the gyroscopes are examined.

- *Thermal Characteristics*

Gyroscope measurements are collected for 6 hours as in the case of accelerometers. Sensor output data is shown with the moving averaged filter output. Temperature dependence has not been observed in the output data (Figure 12 - Gyroscope thermal test data. Outputs are recorded for 6 hours.). Therefore, a thermal error model within this range of temperatures (22ºC to 38ºC) is not recommended.
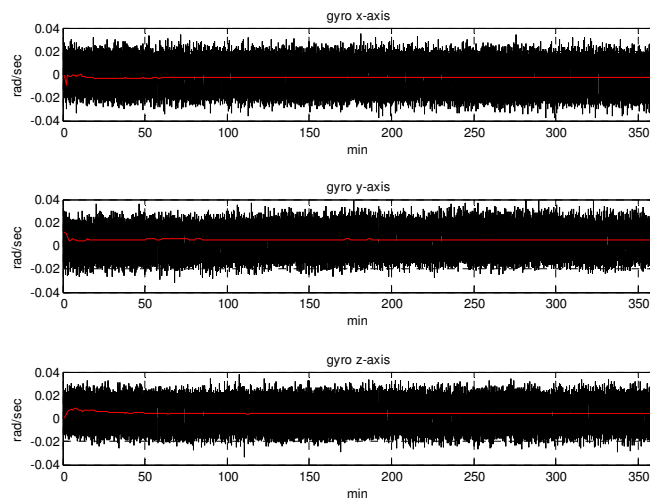
Figure 12 - Gyroscope thermal test data. Outputs are recorded for 6 hours. Data after filtering with a moving average filter is shown in red.

- *Noise Characteristics*

The standard deviation of the long term gyroscope data characterizes the white Gaussian noises, w_B which are found to be around 0.012 rad/sec all axes. The minimum point on the Allan Variance curve is a measure of the drift instability as in the case of accelerometers. Drift instability is calculated to be around 0.2 mrad/sec for all gyroscopes. Allan Variance curve for x-axis gyroscope is given in Figure 13.
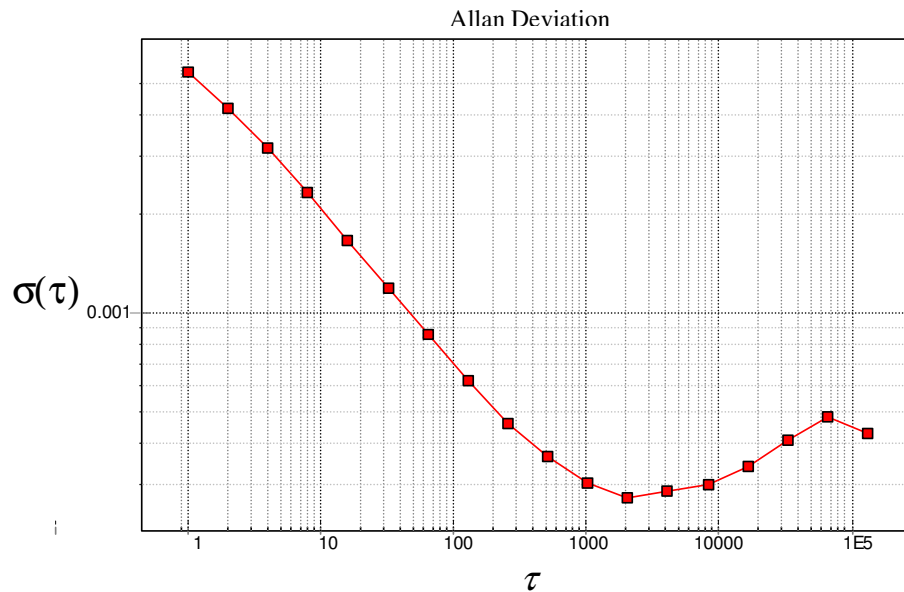
Figure 13 – Allan-Variance curve for gyroscope of x-axis.

2.2 Camera Technology

We now turn our attention to the second type of sensor considered for body-state estimation: the camera. The camera sensor work with the following basic principle: When the camera is pointed to a physical object, an image of this object is formed on a photographic film or an image capture device by means of rays reflected from the object passing through the aperture of the camera lens. The CCD or CMOS

electronic imaging arrays have replaced photographic films with the development of digital technology. Digital images are stored as number arrays where numbers represent the intensity of light exposed on the sensor array.

Cameras are usually classified according to the imaging media, imaging sensor, lens type and frame rate. The quality of the image depends on the properties of the mentioned classifiers including the distortion effect. The accuracy of position estimation from cameras is related to the quality of the images. In this study, a low-quality webcam is used for sensor fusion. The image array is a CMOS sensor with 640 pixel by 480 pixel image size. The mathematical camera model and calibration procedure explained in this section.

2.2.1 Perspective Camera Model

Mathematical camera models represent the mapping of 3D coordinates of a point in the scene to its 2D projection in the *image plane*. The most common model is a first order approximation of the projection and is called the *perspective camera model.* The perspective camera model assumes that the camera is an ideal *pinhole camera* (Figure 14-(a)) where the light coming from the 3D point in the scene passes from an infinitesimal hole and leaves a mark on the image plane which creates the 2D projection coordinate on the image plane [16]. The image plane is *the image sensor* for the case of real cameras. The infinitesimal hole is called *the center of projection* which is assumed to be the lens center in most of the cameras. This is also the origin of the 3D orthogonal camera coordinate system. The *optical axis* of the camera points the viewing direction. The z-axis of the camera coordinate system is assumed to coincide with the optical axis of the camera.
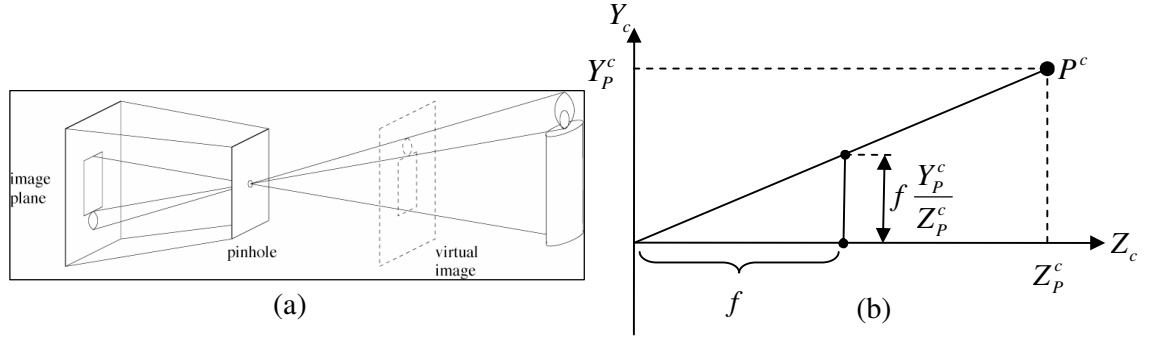
Figure 14 - (a) Pinhole camera model diagram [40] (b) Side view of the camera coordinates showing geometrical relations between the 3D and 2D point coordinates.

The 2D projection of the point is derived by using the similarity of triangles in Figure 14-(b). Here, f is the focal point of the camera. The projection of point P having 3D camera frame coordinates $\begin{bmatrix} X_P^c & Y_P^c & Z_P^c \end{bmatrix}$ on the image plane is given by

$$(u,v) = (f \frac{X_P^c}{Z_P^c}, f \frac{Y_P^c}{Z_P^c}) \tag{6}$$

where u and v represent the components of the *image coordinate frame(i-frame)* with origin on the center of the *image plane*, i.e. the center of projection. However, we will be dealing with *pixel coordinates (p-frame)* since the digital output of the camera is represented by pixel values. Hence, the 2D projection of point P should be

$$(x_{pixel}, y_{pixel}) = (u + u_0, v + v_0) = (f \frac{x_p^c}{z_p^c} + u_0, f \frac{y_p^c}{z_p^c} + v_0) \tag{7}$$

in *p frame* , (u_0, v_0) being the position of center of projection. The coordinate systems that we involve in camera model are visualized in Figure 15.

29
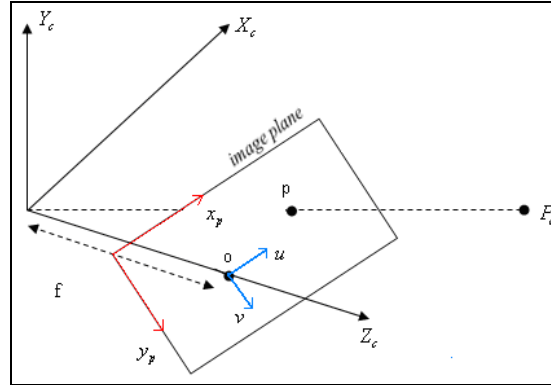
Figure 15 – Camera, image and pixel coordinate frames.

This ideal camera model is converted to a more realistic model by employing terms for non-ideal characteristics of a camera. These include the effective pixel size s_x and s_y, and image plane orientation represented by the skew factor. The aforementioned attributes are collected in a matrix form symbolized by $\mathbf{K}_{int}$ which is multiplied with the position vector of the observed 3D point.

$$\mathbf{K}_{int} = \begin{bmatrix} s_x f & skew\_factor & u0 \\ 0 & s_y f & v0 \\ 0 & 0 & 1 \end{bmatrix} \tag{8}$$

$$(x_p, y_p) = \mathbf{K}_{int}\mathbf{P^c} \tag{9}$$

Additionally, non-linear image distortion model can be utilized to express the non-ideal lens properties. In more recent works, a distortion model is also suggested by introducing non-linear coefficients to the camera model.

2.2.2 Camera Calibration

Camera calibration can be defined as the determination of internal and external parameters of a camera. By internal calibration, we refer to the determination of *pinhole camera model* parameters, i.e. $\mathbf{K}_{int}$ explained in 2.2.1. $\mathbf{K}_{int}$ defines the relationship between the *c frame* and *p frame*. However, point *P* is represented in *g frame* since it is not possible to measure the distance from the center of the camera to the point P. Hence, we should know the transformation between the *c frame* and *g frame* which is called the external projection. Determination of the position of camera in *g frame* and the rotation between the frames are calculated via external calibration. These are represented by respectively. The equation to calculate the c-frame coordinates of point P is given in Eqn.(10).

$$\begin{bmatrix} X_p^c \\ Y_p^c \\ Z_p^c \end{bmatrix} = \mathbf{R}_{ext} \begin{bmatrix} X_p^g \\ Y_p^g \\ Z_p^g \end{bmatrix} + \mathbf{t} \tag{10}$$

The relationship given in equation (10) can be represented with a single matrix multiplication by combining *t* and $\mathbf{R}_{ext}$ in a 3x4 matrix $\begin{bmatrix} \mathbf{R}_{ext} \mid \mathbf{t} \end{bmatrix}$ and multiplying the resultant with employing *homogeneous coordinates,* a 4x1 vector. Homogeneous coordinates are formed with augmenting "1" at the end of the coordinate vector.

$$\begin{bmatrix} mx_p \\ my_p \\ m \end{bmatrix} = \mathbf{K}_{int} \begin{bmatrix} \mathbf{R}_{ext} \mid \mathbf{t} \end{bmatrix} \begin{bmatrix} X_p^g \\ Y_p^g \\ Z_p^g \\ 1 \end{bmatrix} \tag{11}$$

The calculated pixel coordinate vector from Eqn.(11) is weighted by a factor of *m* which is the 3rd component. By dividing the first two components of the vector, pixel coordinates are obtained.

The camera calibration algorithm and procedure is explained in section 2.2.3.

2.2.3 Camera Calibration Procedure

Intrinsic and extrinsic parameters of the camera are obtained by utilizing the Camera Calibration Toolbox for MATLAB developed at vision laboratory of CalTech [19]. The camera model is a pinhole camera model with radial and tangential parameters. Distortion model is not utilized in the initialization step. The main internal parameters are estimated using images of a planar checkerboard pattern (Figure 16). This pattern provides a number of points for minimization of the re-projection error.
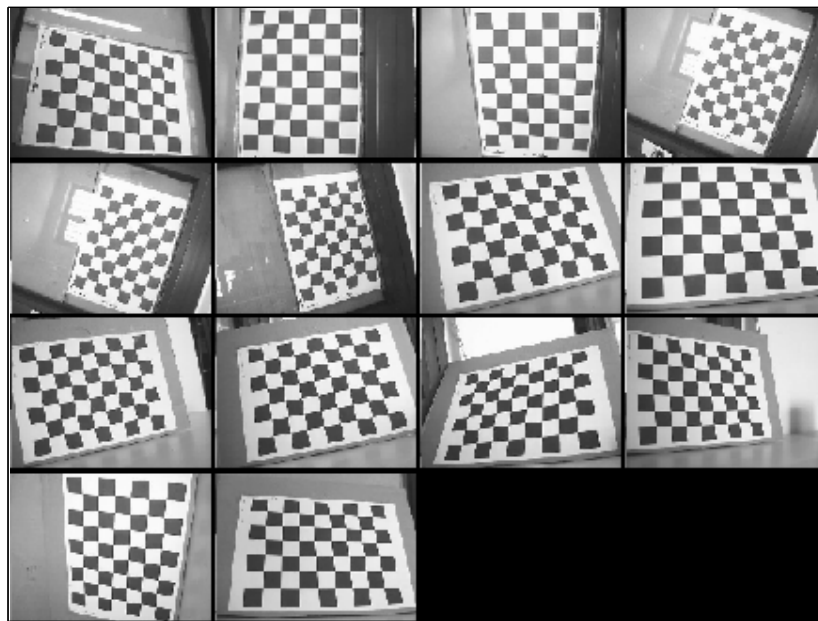
Figure 16 – Checkerboard pattern images used for intrinsic calibration

The corners in the image are extracted and reprojection error is minimized by gradient-descent algorithm to find the internal camera. The parameters are supplied with the uncertainties. The average pixel error is also calculated. One of the images with the extracted and projected corners and the distribution of reprojection pixel error are shown in Figure 17.

(a)   (b)
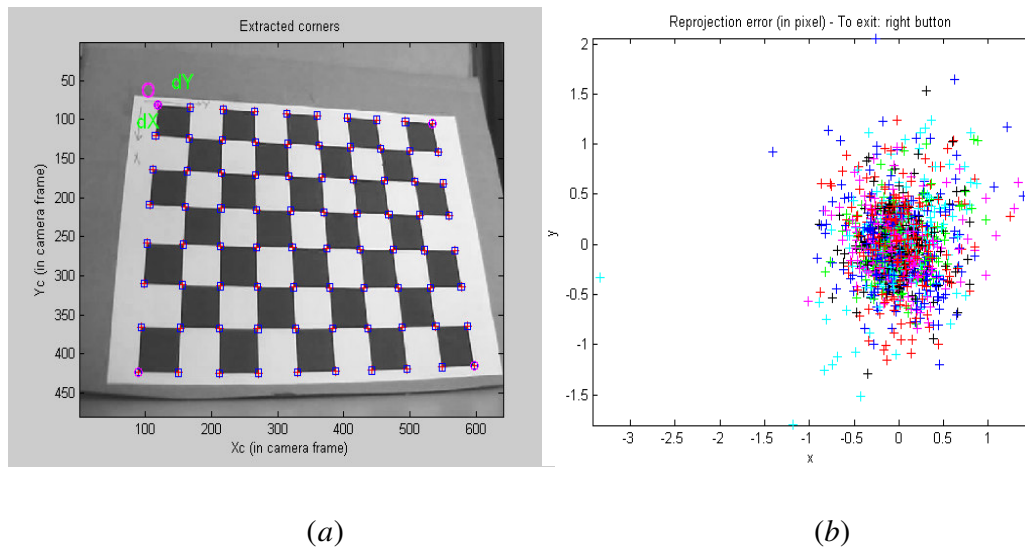
Figure 17-Extracted (α) and reprojected (b) image points for calibration of the webcam. Reprojection error is given in pixels. The average pixel error is 0.4 pixels in x-direction and 0.6 pixels in y-direction.

Internal camera parameters for Apache webcam are obtained as follows:

Focal Length: fc = [776.60959   778.43741] ± [3.41506   3.47197]

Principal point: cc = [333.94725   217.49120] ± [3.59244   3.46439]

Skew: alpha_c = [0.00000] ± [0.00000]   =>

Distortion: kc = [-0.16135   0.02013   -0.00327   -0.00284]

                              ± [0.01628 0.07772   0.00089   0.00089]

Pixel error: err = [0.36118   0.41118]

The unit for the internal parameter values is "one pixel length", i.e. focal length is equal to the length of 776.6 pixels. The average pixel error is obtained to be 0.3 pixels for x-axis and 0.6 pixels for y-axis. Apart from the main internal parameters; focal length, center pixel (principal point) and the skew coefficient, the distortion parameters are also calculated. However distortion model is highly non-linear. The toolbox has a function to un-distort the taken images according to the obtained distortion parameters. To exclude the distortion model, we use the undistorted images in algorithm.

The external camera parameters of the webcam are calculated at in the experimental setup. The corner of the checkerboard pattern is marked as the origin of the global coordinate frame. The rotation and translation matrices are obtained as follows:

Translation vector: Tc_ext = [-139.026981   -85.305398   360.320151]

Rotation matrix: Rc_ext = [0.012290   0.996590   -0.081590

                            0.999901   0.011692   -0.007805

                       -0.006824   -0.081678   -0.996635]

The internal and external parameters will be utilized in joint calibration of IMU and camera which is explained in the next section.

2.3   Joint Calibration of IMU and Camera

We have mentioned earlier that IMU-Camera calibration is an active research area. Recently two methods come forward: vanishing point approach and Kalman Filter approach. In this study we preferred vanishing point approach since the parameter estimation covariance is shown to be smaller than that of Kalman Filter calibration methods. The algorithm developer J.Lobo has presented a number of papers on vanishing point approach [22],[23]and presented an open source code for MATLAB[24]. This toolbox is compatible with the Camera Calibration Toolbox and uses the internal and external camera parameters obtained.

The parallel lines in a real scene intersect at a finite point in images. The intersection point is called the vanishing points. In the 2D projection of a planar grid such as a checkerboard pattern, there are two intersection points created by the parallels and they define a plane. The normal of this plane is called the vanishing line. When a vertical pattern is observed by the camera, the vanishing line provides a reference for the vertical.

Assuming that the IMU and the camera are rigidly attached to each other, we can obtain several measurements for vertical reference from both sensors. Using the vanishing lines and the effect of gravitational acceleration, it is possible to estimate the angular rotation between the sensor pair.

The translation between the camera and the IMU is inconsiderable for the experiments considered in this study. The angular velocity does not change weather it is measured form the center of the camera, center of rotation or any other place on the rotating plane. Hence we will not deal with the translation between the sensor pair.

The rotation between the sensors is calculated in a quaternion form in the mentioned toolbox. The uncertainty in the quaternion estimate is also calculated. The quaternion matrix is converted to rotation matrix with the relation given in Eqn. (13).

$$q = q_1 + q_2 i + q_3 j + q_4 k \tag{12}$$

$$\mathbf{C} = \begin{bmatrix} q1^2 + q2^2 - q3^2 - q4^2 & 2(q2q3 - q1q4), & 2(q1q3 + q2q4); \\ 2(q1q4 + q2q3) & q1^2 - q2^2 + q3^2 - q4^2 & 2(q3q4 - q1q2) \\ 2(q2q4 - q1q3) & 2(q1q2 + q3q4) & q1^2 - q2^2 - q3^2 + q4^2 \end{bmatrix} \tag{13}$$

The quaternion vector and the associated direction cosine matrix are given in equations (14) and (15).

$$\mathbf{q} = 0.999911 - 6.022641 \times 10^{-5} \mathbf{i} - 0.0133002 \mathbf{j} - 0.000185 \mathbf{k} \tag{14}$$

$$\mathbf{C_b^c} = \begin{bmatrix} -0.999605 & 0.009422 & -0.026476 \\ 0.008682 & 0.999572 & 0.027935 \\ 0.026728 & 0.027694 & -0.999259 \end{bmatrix} \tag{15}$$

The outputs of camera calibration and joint IMU-camera calibration provide us the transformation matrices between the camera-global (C_c^g) and camera-IMU frames (C_b^c). The transformation between the IMU and global frame is calculated by the multiplication of these matrices (Eqn.(16)).

$$\mathbf{C_b^g} = \mathbf{C_c^g} \mathbf{C_b^c} \tag{16}$$

Global coordinate frame, camera coordinate frame and body coordinate frame are demonstrated in Figure 18 using the calibration parameters obtained.
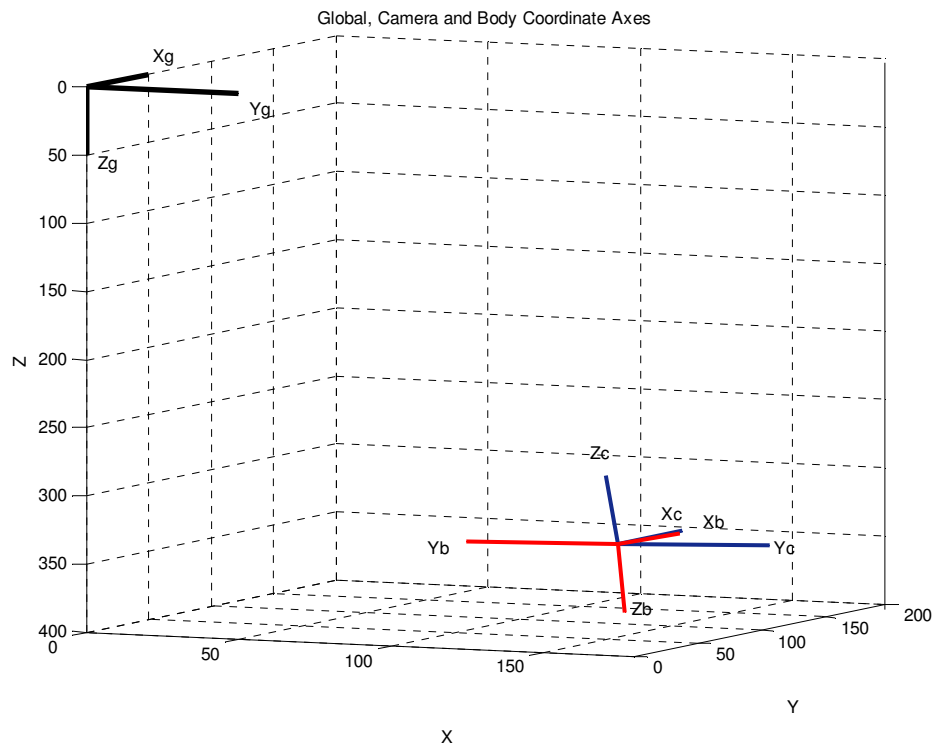
Figure 18 – Demonstration of coordinate frame locations and orientations with the calibration parameters obtained.

CHAPTER 3

KALMAN FILTERING FRAMEWORK FOR STATE ESTIMATION

Having reviewed the sensors taking part in our work, we now focus on the mathematical mechanism that we have elected to use for the fusion of these sensors. This chapter briefly reviews the basics of the Kalman Filter, the Extended Kalman Filter and the Indirect (Error State) Kalman Filter for state estimation applications. Later in Chapter 4, the dynamical system model of our moving platform will be developed in accordance with the framework presented in this chapter.

3.1   The Kalman Filter

The Kalman Filter (KF) is the optimal minimum mean square error state estimator for linear dynamic systems driven by white Gaussian noise. Kalman Filter is also considered to be the best linear state estimator (or in the sense of Minimum Mean Square Error) for linear dynamical systems driven by non-Gaussian random variables [39].

KF recursively estimates the state of a dynamic system based on a sequence of noisy measurements and starting from an initial condition which is also assumed to be a random variable. The linear dynamic system is modeled as a Markov Process which presumes that the current state depends only on the previous state of the dynamic system.

The discrete-time state space representation of the next true state $x(k+1)$ of the dynamic system evolving from the previous state $x(k)$ is given in Eqn.(17) where

F(k) is the state transition matrix, **G(k)** is the control-input matrix, *u(k)* is the input and *w(k)* is the additive white Gaussian process noise with zero mean and covariance matrix **Q(k)**(Eqn.(19)).

$$x(k+1) = \mathbf{F(k)}x(k) + \mathbf{G(k)}u(k) + w(k) \tag{17}$$

Measurement at time k is given by the model in Eqn(18) *H(k)* being the observation model and *v(k)*, the measurement noise with zero mean and covariance *R(k)*(Eqn(19)). Apart from their Gaussian properties, process noise and measurement noise are also assumed to be *mutually independent*.

$$z(k) = \mathbf{H(k)}x(k) + v(k) \tag{18}$$

$$w(k) \sim N(0, Q(k)), \; v(k) \sim N(0, R(k)) \tag{19}$$

State estimation is conducted considering the state space representation of the dynamic system in a two phase cycle with the details explained below [39].

(1) First phase is the state and measurement prediction (time update) phase where *a priori state estimate* is

$$\hat{x}(k+1|k) = \mathbf{F(k)}\hat{x}(k|k) + \mathbf{G(k)}u(k) \tag{20}$$

given the previous measurements and the state space model of the system which can be whether time-dependent of time independent. The initial state estimate is given by

$$E[x(0)|Z^0] = \hat{x}(0|0) \tag{21}$$

The state prediction covariance is the covariance of the predicted state (Eqn. (22)) given the previous measurements Z^k and updated at each time step according to

39

Eqn(23) with the initial covariance matrix **P(0|0)** which is assumed to be known initially.

$$\mathbf{P(k+1|k)} = \text{cov}[\hat{x}(k+1|k)|Z^k] \tag{22}$$

$$\mathbf{P(k+1|k)} = \mathbf{F(k)P(k|k)F(k)}^T + \mathbf{Q(k)} \tag{23}$$

$$\text{cov}[x(0)|Z^0] = P(0|0) \tag{24}$$

(2) In second phase, state update (measurement update) or *a posteriori* state estimate is calculated considering the difference between the actual measurement $z(k)$ and the measurement prediction $\hat{z}(k)$ given in (25). The difference is called *the innovation* or *the residual* (Eqn(26)) and has covariance $S(k)$ given in Eqn (27).

$$\hat{z}(k+1|k) = \mathbf{H(k+1)}\hat{x}(k+1|k) \tag{25}$$

$$\tilde{y}(k+1) = z(k+1) - \hat{z}(k+1|k) \tag{26}$$

$$\mathbf{S(k+1|k)} = \mathbf{H(k)P(k+1|k)H(k)}^T + \mathbf{R(k)} \tag{27}$$

$$\mathbf{K(k+1)} = \mathbf{P(k+1|k)H(k+1)^T S(k+1)^{-1}} \tag{28}$$

Finally, the state estimate and the state covariance are updated according to equations (29) and (30) where $K(k)$ is the weighting matrix (Eqn (28)).

$$\hat{x}(k+1|k+1) = \hat{x}(k+1|k) + \mathbf{K(k+1)}\tilde{y}(k+1) \tag{29}$$

$$\mathbf{P(k+1|k+1)} = \mathbf{P(k+1|k)} - \mathbf{K(k+1)S(k+1)K(k+1)^T} \tag{30}$$

3.2 Extended Kalman Filter

It has been mentioned that Kalman Filter is the optimal state estimator for linear systems with driven by white Gaussian noise. In real life conditions it is usually non-trivial to represent systems and/or measurements by linear models. Extended Kalman Filter (EKF) is developed as an extension to systems that can be modeled by a non-linear but differentiable state transition function $f(k, x(k), u(k))$ and observation function $h(k, x(k))$. Process and observation noises are still modeled as Gaussian random variables with the statistical properties given by Eqn.(19) in Section 3.1.

$$x(k+1) = f(k, x(k), u(k)) + w(k) \qquad (31)$$

$$z(k) = h(k, x(k)) + v(k) \qquad (32)$$

The dynamic system equations demonstrated in equations (31) and (32) and are used to estimate and update the *a priori* state estimate (eqn. (33)) and measurement estimate (eqn.(34)).

$$\hat{x}(k+1|k) = f(k, \hat{x}(k|k), u(k)) + w(k) \qquad (33)$$

$$\hat{z}(k+1|k) = h(k, \hat{x}(k+1|k)) + v(k) \qquad (34)$$

The Jacobian of the state transition function *f* and observation function *h* are used calculated at each step since the covariance cannot be calculated explicitly form the functions *f* and *h*. Hence state transition matrix and the observation matrix becomes

41

$$\mathbf{F}_k = \left. \frac{\partial f}{\partial x} \right|_{\hat{x}(k-1|k-1), u(k)} \tag{35}$$

$$\mathbf{H_k} = \left. \frac{\partial h}{\partial x} \right|_{\hat{x}(k|k-1)} \tag{36}$$

by linearizing f at the state estimate and h at the state prediction.

EKF is the *non-optimal* state estimator due to the fact that the Jacobians of the state transition and observation functions are utilized instead of the original functions. Any modeling or initial state estimate error may cause the EKF to diverge. Nevertheless, EKF can practically yield satisfactory results and hence is widely accepted for body state estimation applications.

3.3   Indirect (Error State) Kalman Filter

Using Kalman Filters for body state estimation require modeling of the dynamical system which can be very complicated. There may be high number of states and the model has to be updated whenever a change occurs in the platform. In addition, if the system is highly non-linear Extended Kalman Filter may diverge. Indirect Kalman Filter structure estimates the error in the navigation variables using the difference between the calculated navigation variables by integration and the aiding sensor [41]. Inertial navigation equations are updated outside the filter and dynamical modeling is not required. The block diagram of the Direct Kalman Filter and indirect Kalman Filter for sensor fusion is demonstrated in Figure 16 and Figure 20 respectively.
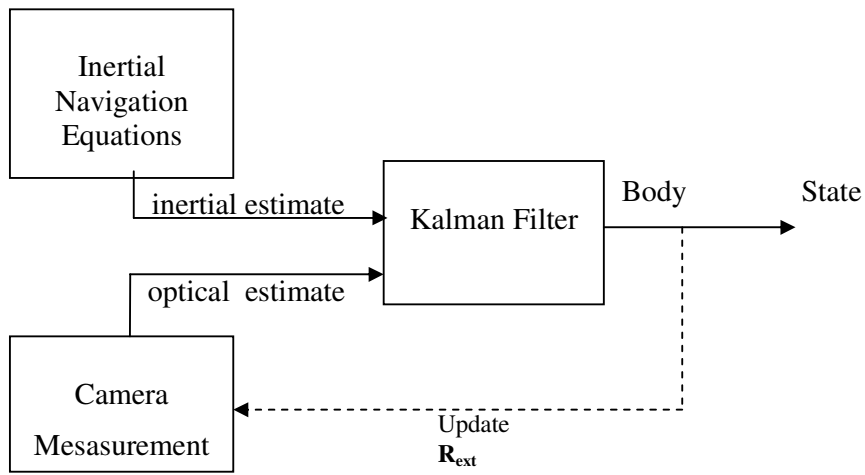
Figure 19 – Kalman Filter structure for sensor fusion
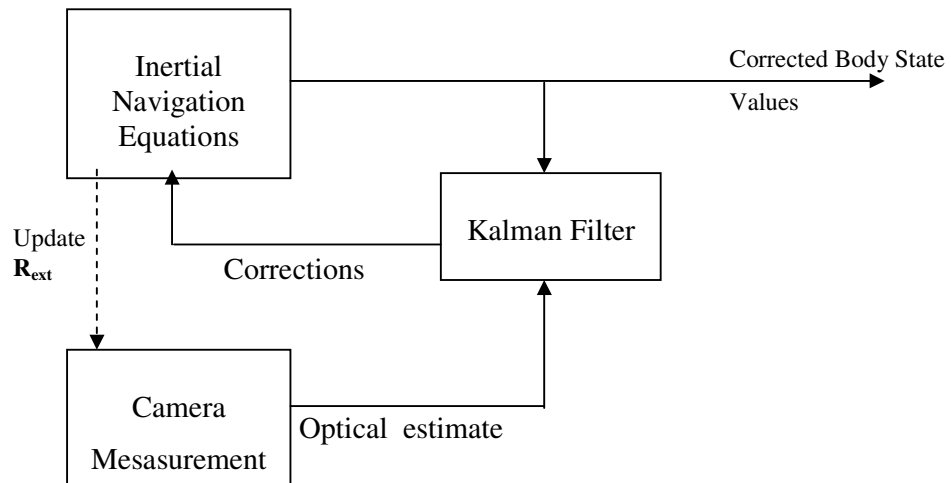
Figure 20 – Indirect Kalman Filter structure for body state estimation using inertial sensors and cameras.

State space equations of indirect Kalman Filter are formed by expressing the change of errors with respect to time. In equation(37), $\hat{x}$ is the estimate of the variable of

interest, x is the true value of the variable and δx is the error in the estimate. The error propagates in time according to equation(38). Kalman Filter state update and time update stages are processes with the measurement residual (Eqn.(39)) where $\tilde{x}$ is the measured quantity corrupted by white Gaussian noise with variance R. The measurement equation is expressed in matrix form in Equation(40). The state vector is corrected by weighing the measurement residual with Kalman Gain, **K** (Equation(41)).

$$\hat{x} = x + \delta x \tag{37}$$

$$\delta x(k+1) = \mathbf{F_e} \delta x(k) + v \tag{38}$$

$$z = \hat{x} - \tilde{x} \tag{39}$$

$$z = \mathbf{H} \delta x + w \tag{40}$$

$$\hat{x} = \hat{x} - \mathbf{K} z \tag{41}$$

In our case, the angular position is calculated using the current gyroscope output and then corrected by the angular position error estimate. The differential equation for angular position error is found by subtracting those equations. The actual angular position differential equation and angular position calculated from the sensor outputs are given in Eqn.(42) and Eqn.(43) respectively. The differential equation for angular position error is found by subtracting those equations (Eqn.(44)).

$$\dot{\theta}_{true} = \omega_{true} \tag{42}$$

$$\dot{\theta}_{inertial} = \omega_{gyro} \tag{43}$$

$$\delta\dot{\theta} = \omega_{true} - \omega_{gyro}$$
$$\delta\dot{\theta} = \delta\omega \tag{44}$$

The error on angular velocity measurement is given by the gyroscope error equation presented in Section 2.1.2, which is added to the error state vector. The camera measurements are nonlinear hence the Jacobian of the measurement equations is calculated (Eqn.(45)).

$$\mathbf{J_k} = \frac{\partial h}{\partial x}\bigg|_{\hat{x}(k|k-1)} \tag{45}$$

The measurement equation becomes:

$$\delta z = \mathbf{J}\delta\mathbf{x} \tag{46}$$

The error estimates are subtracted from the calculated variables to get the corrected body state estimates (Eqn.(47)).

$$\theta(k+1) = \theta(k+1) - \delta\theta \tag{47}$$

CHAPTER 4

PROBLEM FORMULATION

We have covered the background on sensors and the fusion framework. In the present chapter, we attempt to formulate the particular problem that we are interested in, namely estimating the state of a moving platform by joint means of an IMU sensor and a camera sensor. This consists of two main steps: The derivation of moving platform state-space dynamic model and the derivation of the sensor measurement model. Collectively, these set of equations will form system and measurement model for the Kalman Filter.

4.1 Coordinate Systems

Study of moving bodies in space required careful definition of a number of coordinate systems to mathematically represent the state. We proceed as follows:

Global coordinate system (g frame): Can be any stationary 3D coordinate system defined in the scene. In this work, the origin of the stationary *g-frame* is chosen to be the center of the rate table for simulations. As illustrated in Figure 21, the X_g and Y_g axis are aligned with the rate table plane and Z_g axis is pointing up from the table plane completing the right handed coordinate system.
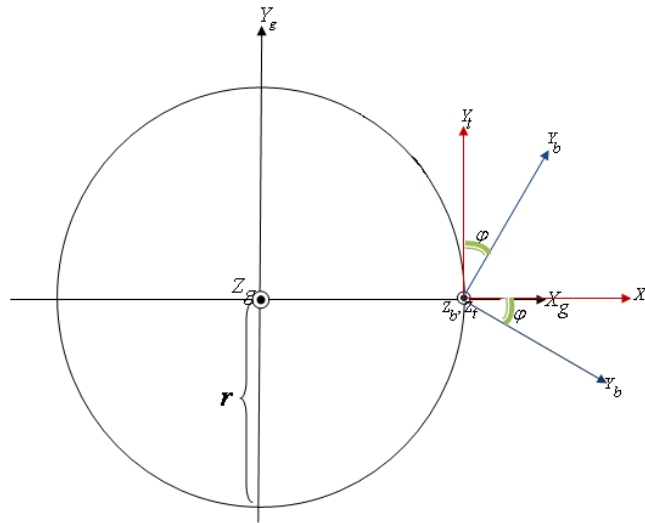
Figure 21 – Coordinate system definitions

Body coordinate frame (b frame): 3D coordinate system fixed to the moving body. The moving body in this thesis is the inertial measurement unit. Hence X_b, Y_b and Z_b are defined on the IMU case where x-axis points forward, y-axis points right and z-axis points out of the body, in the gravity direction.

Tangential coordinate frame (t frame): Rotating 3D coordinate frame defined for IMU measurement simulations. Y_t is defined to be always tangential to rotation arc and Z_t points out of the table plane as shown in Figure 21.

Camera coordinate frame (c frame): 3D coordinate system fixed to the camera center. The origin of the *c frame* and the *b frame* are assumed to be coincident. The z-axis of the *c frame* is aligned with the optical axes of the camera.

Pixel coordinates (p frame): 2D coordinate system defined on the image with the origin on the top left corner of the image plane.
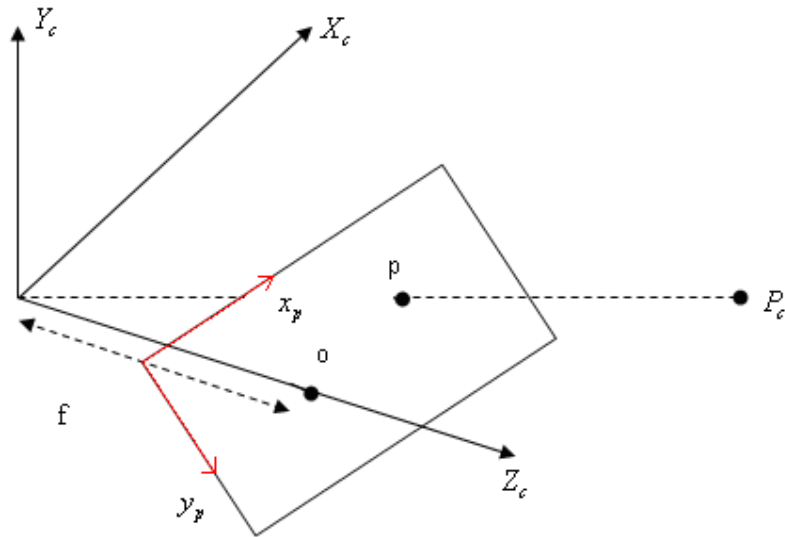
Figure 22 – Camera and pixel coordinate systems

Each sensor takes the measurements according to its own coordinate system. However it is necessary to perform calculations on a common frame. A vector in a particular coordinate system can be represented in another system by means of coordinate transformations. There are some methods to achieve this conversion such as using direction cosines, quaternions and exponential coordinates which involve the angle relations between the coordinate axes of the systems. These relations are calculated through the calibration process which we are explained in detail in section 2.2.3.

In this study, we use direction cosine matrices to express the translation between the coordinate systems. Direction cosine matrices are related with Euler Angles which describe the orientation of a coordinate frame relative to another coordinate frame. This orientation is represented by three rotations, one rotation per axis. φ, θ and

48

ϕ are the rotations around the first, second and third axes respectively. Equation (48) demonstrates the formation of a direction cosine matrix from some general coordinate system a to another general coordinate system b. The transpose of the matrix is equal to the opposite transformation.

$$C_a^b = \begin{bmatrix} 1 & 0 & 0 \\ 0 & \cos\phi & -\sin\phi \\ 0 & \sin\phi & \cos\phi \end{bmatrix} \begin{bmatrix} \cos\theta & 0 & \sin\theta \\ 0 & 1 & 0 \\ -\sin\theta & 0 & \cos\theta \end{bmatrix} \begin{bmatrix} \cos\varphi & -\sin\varphi & 0 \\ \sin\varphi & \cos\varphi & 0 \\ 0 & 0 & 1 \end{bmatrix} \quad (48)$$

4.2   State Space Formulation of the Moving System

Kalman Filter formulation requires the dynamical system and the measurements to be modeled. Our moving system is a rate table which will provide the system matrix. The measurements are obtained from the gyroscope and camera measurements. The camera measurements are non-linear. The equations and the linearization procedure is explained in this section.

4.2.1   System dynamic equations

The input and the output of the rate table is the angular velocity Motion control is through cascaded velocity and current loops which have a PI controller structure. The velocity loop is responsible for generating the current necessary for the needed torque [45]. The motor model is the conventional DC motor model [46]. The velocity loop, current loop and the motor model parameters are supplied by the manufacturer.
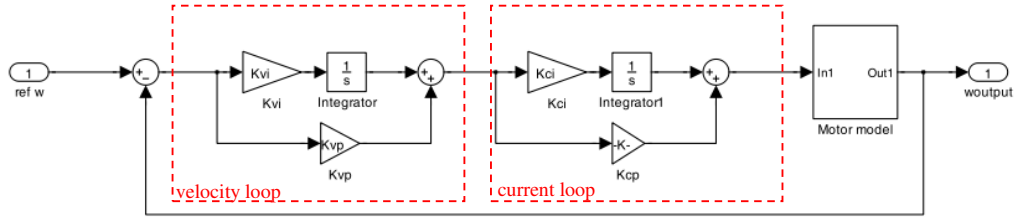
Figure 23- Block Diagram of Rate Table Model with an angular velocity reference input and the angular velocity output

The states of the state space formulation of the block diagram given in Figure 23 are the angular velocity output, the integral of the difference between angular velocity output and the commanded angular velocity input, and the integral of the current (eqn.(50)).

$$\dot{x}(t) = \mathbf{A}x(t) + \mathbf{B}w_{in}(t)$$
$$y(t) = \mathbf{C}x(t)$$
(49)

$$x(t) = \begin{bmatrix} \omega & \int(\omega - w_{in}) & \int i \end{bmatrix}^{T}$$
(50)

We use the observable form of the system matrix A and angular position is added to the states. The continuous time state transition matrix and the control input matrix are given by equations (51) and (52) respectively.

$$\mathbf{A} = \begin{bmatrix} \dfrac{-b - K_{vp} \times K_{cp}}{J_m} & 1 & 0 & 0 \\ \dfrac{-K_{vp} \times K_{ci} - K_{vi} \times K_{cp}}{J_m} & 0 & 1 & 0 \\ \dfrac{-K_{vi} \times K_{ci}}{J_m} & 0 & 0 & 0 \\ 1 & 0 & 0 & 0 \end{bmatrix}$$
(51)

50

$$\mathbf{B} = \left[\frac{K_{vp} \times K_{cp}}{J_m} \quad \frac{-K_{vp} \times K_{ci} - K_{vi} \times K_{cp}}{J_m} \quad \frac{K_{vi} \times K_{ci}}{J_m} \quad 0 \right]^T \tag{52}$$

The Kalman Filter is to be implemented in discrete time making it necessary to find the discrete time representation of the system (Eqn.(53)). The continuous time expressions are converted to their discrete time equivalents with the sampling time dt. In this study, sampling time is chosen to be 0.01 seconds, in consistent with IMU sampling intervals.

$$\begin{aligned} x(k+1) &= \mathbf{F}x(k) + \mathbf{G}w_{in}(k) \\ y(k+1) &= \mathbf{H}x(k+1) \end{aligned} \tag{53}$$

$$\mathbf{F} = \exp(\mathbf{A} \times dt) \tag{54}$$

$$\mathbf{G} = (\int_t^{t+\Delta t} e^{\mathbf{A}\tau} d\tau) \times \mathbf{B} \tag{55}$$

The initial state estimate covariance $\mathbf{P(0|0)}$ is the zero for all states for simulations since the initial state is known perfectly. For the real case, initial velocity estimate is known to be zero, perfectly for the angular velocity since the system is at rest initially. On the other hand, the initial position estimate in hardware experiments is known to the extent of the uncertainties of calibration procedure, which obtained to be 0.5 degrees (0.01 rad). $\mathbf{P}$ is updated at each time step according to (23).

$$\mathbf{P(0|0)} = \begin{pmatrix} 0 & 0 & 0 & 0 \\ 0 & 0 & 0 & 0 \\ 0 & 0 & 0 & 0 \\ 0 & 0 & 0 & 0.01 \end{pmatrix} \tag{56}$$

The process noise covariance matrix $\mathbf{Q(k)}$ is determined considering the rate table output velocity and position noise characteristics for both simulation and hardware esperiments. The noise angular position output is observed to be 0.001rad.

51

$$\mathbf{Q(k)} = E\left[v(k)v(k)^T \right] \tag{57}$$

4.2.2 Measurement Equations

In this section, we will explain the measurement equations used for the body state estimation strategies: gyroscope only, camera only and the two sensors together.

4.2.2.1 Measurement Equations for KF-G

The gyroscope measures the angular velocity which is nothing but the first state of our state space formulation. The only important thing is to express the angular velocity vector in global coordinates. We should multiply the gyroscope measurement with the coordinate transformation matrix relating the body coordinates with the global coordinates.

$$\omega_m = C_b^g \omega_{gyro} \tag{58}$$

The coordinate transformation matrix change in time since the body is moving. They are updated using the latest state estimate at each step with the expression given in equation(59)

$$C_b^g(new) = C_b^g \Omega_b \tag{59}$$

Hence, the measurement equation of the KF-G is Eqn.(60), $\mathbf{H}$ being the measurement matrix. The Kalman Filter update rate is equal to the IMU sampling rate which is 100Hz.

$$y(k+1) = \mathbf{H}x(k+1)$$
$$H = \begin{bmatrix} 1 & 0 & 0 & 0 \end{bmatrix} \tag{60}$$

52

The measurement covariance value is set using the standard deviation of gyroscope measurements during calibration tests.

$$\mathbf{R(k)} = E\left[w(k)w(k)^T \right]$$
$$\mathbf{R(k)} = \left[\sigma^2_{gyro} \right] \tag{61}$$

4.2.2.2 Measurement Equations for KF-C

The 2D projection of point P in the scene is fed to KF-C as measurements. The 3D global coordinates of the point of interest is projected on the image plane with equation (11) explained in section 2.2.1. This measurement is non-linear hence we should calculate the Jacobian of the measurement function. At every time step, the measurement estimation is calculated with equation (62) where the measurement matrix H is equal to the Jacobian of the measurement function.

$$y(k) = h(x(k), u(k)) + v_k \tag{62}$$

$$\mathbf{H} = \mathbf{J(h)} = \frac{\partial}{\partial x} h(x, u)$$
$$\mathbf{J} = \begin{bmatrix} 0 & 0 & 0 & \dfrac{\partial p_x}{\partial \theta} \\ 0 & 0 & 0 & \dfrac{\partial p_y}{\partial \theta} \end{bmatrix} \tag{63}$$

The derivative of the measurement is zero with respect to all variables except for the angular position. Angular position of the camera is acting on the coordinate transformation matrix and the position of the camera coordinates with respect to the global coordinates. This step is handled MATLAB hence is not included here.

The measurement covariance matrix is set considering the typical pixel error value for cameras. For real experiments, this value is equal to the average pixel error calculated in internal calibration procedure (Eqn.(64)).

$$\mathbf{R(k)} = \begin{bmatrix} \sigma_{cam}^2 & 0 \\ 0 & \sigma_{cam}^2 \end{bmatrix} \tag{64}$$

The Kalman Filter update rate is equal to the camera sampling rate which is 30 frames/sec.

4.2.2.3 Measurement Equations for KF-GC

The measurement matrix for the fusion case is also non-linear since cameras are included in the system. The measurement statement of the gyroscope is just concatenated to the Jacobian matrix. The Kalman Filter is updated whenever a measurement is ready, i.e. when a measurement is received from the IMU, and/or the camera.

$$\mathbf{J} = \begin{bmatrix} 0 & 0 & 0 & \dfrac{\partial p_x}{\partial \theta} \\ 0 & 0 & 0 & \dfrac{\partial p_x}{\partial \theta} \\ 1 & 0 & 0 & 0 \end{bmatrix} \tag{65}$$

The measurement covariance matrix is formed form the camera pixel error and gyroscope outputs standard deviation values. R is a 3x3 matrix with sensor error covariances on the diagonals (Eqn.(66)).

$$\mathbf{R} = \begin{bmatrix} \sigma_{cam}^2 & 0 & 0 \\ 0 & \sigma_{cam}^2 & 0 \\ 0 & 0 & \sigma_{gyro}^2 \end{bmatrix} \qquad (66)$$

4.2.2.4 Outlier Rejection

An outlier is defined as an observation lying at an abnormal distance from other values of a random sequence [47]. The measurements collected from the sensors include randomly distributed errors. A measurement may have very noisy measurements at random time instants, which are not likely to belong to the set of other measurements. To negate such measurements, a "circle of confidence" is defined and the outliers are rejected. The distance measure is chose to be the Mahalanobis Distance (MD). This distance measure takes the difference between the measurement and the estimated measurement, i.e. the innovation, and the innovation covariance into consideration (Eqn.(67)).

$$MD^2 = \left(z_k - \hat{z}_k \right)^T \mathbf{S}^{-1} \left(z_k - \hat{z}_k \right) \qquad (67)$$

MD is calculated for every measurement. The measurements with Mahalanobis Distance under the threshold are processed by the algorithm.

The following two chapters will now present first our simulation based experimental setup and results, followed by the real hardware setup and results.

CHAPTER 5

SIMULATION EXPERIMENTS

The simulations were intended to first test the feasibility of the basic principles of camera-IMU sensor fusion. They were conducted first and successful results during simulation experiments provided an opportunity to test these principles on an actual hardware setup. Also, simulations render the study more accessible since they can be comparatively easy to replicate. The simulation environment also provided us a controlled environment to perform sensitivity experiments.

5.1   Simulation Set-up

Since the aim was ultimately to verify simulation results by real hardware experiments, the simulation set-up is modelled with consideration of the hardware experimental set-up. We have deliberately chosen a simple, single DOF motion which can be feasibly realized in hardware. In our set-up, the camera - IMU pair is rotating on a single axis, rotating *rate-table* whose mathematical model is known. The sensor outputs are simulated using the set-up geometry and the sensor models. A top-view drawing of the rate table is shown in Figure 24.
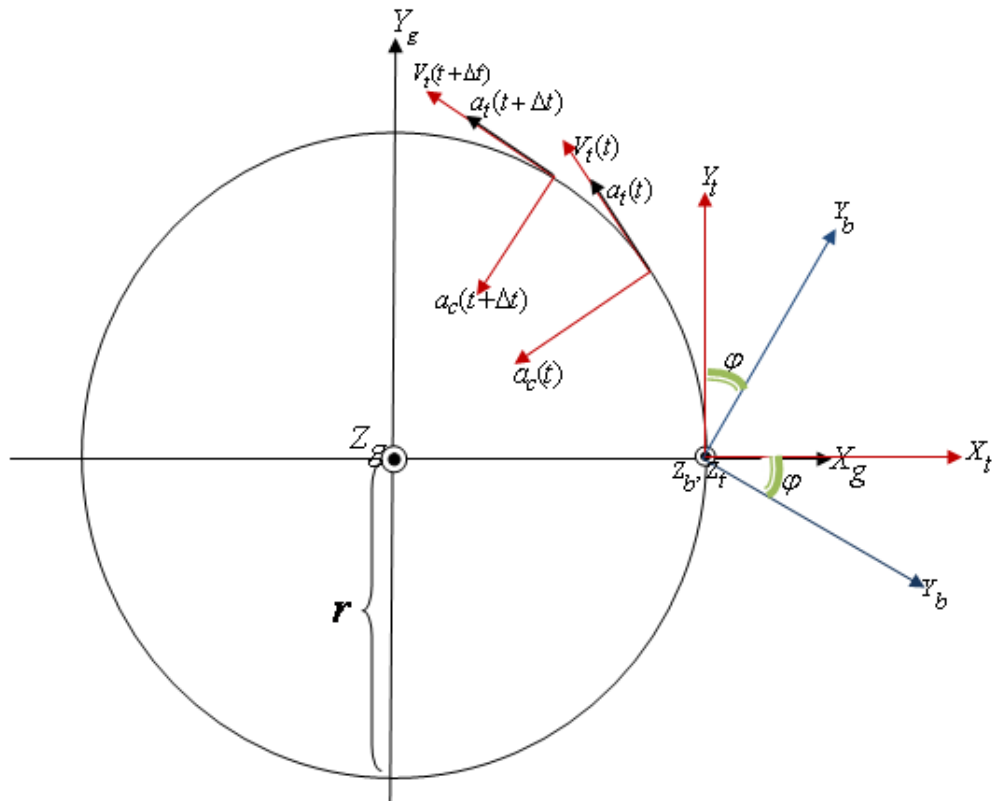
Figure 24 – Rate table top view demonstrated with global, body and tangential coordinate systems

The sensor data are generated with the assumption that the transformation matrices between the coordinate systems are perfectly known. But the sensor fusion algorithms are run such that we know the calibration parameters with some error. . Data generation and the description of the simulations are given in proceeding sections.

5.2   IMU Data Generation

Inertial measurement unit data is simulated building the system dynamic model and IMU error model on Simulink platform. We illustrate the high level block diagram of the model in Figure 25 and give the details in the following paragraphs.

We have derived the state space model of the rate table in Section 4.2.1 which is represented by the "rate table dynamics" block in Figure 25. Rate table reference input *w_in* is fed to this block to obtain the response of the table, *w*.
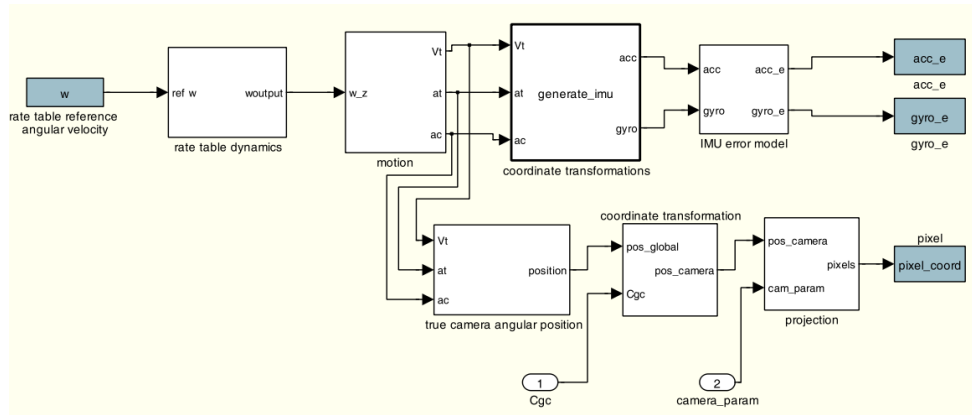
Figure 25 – Simulink model for IMU and camera measurement simulation. The reference input is fed to the rate table model. Actual accelerations,veleocities and positions are calculated. Using coordinate transformations and sensor models, realistic data is obtained.

Before moving on to the next block in the model, we will find it useful to remember the relationship between the angular velocity, tangential velocity, tangential acceleration and centripetal acceleration:

$$V_{tangential} = V_t = rw \tag{68}$$

58

$$a_{tangential} = a_t = r\frac{dw}{dt} \qquad (69)$$

$$a_{centripetal} = a_c = w^2 r \qquad (70)$$

where r is the radius of the rotation arc and w is the rotational velocity experienced by the body. "motion" block of the Simulink model is responsible for calculating the outputs of equations (68),(69) and (70) which are fed to the "coordinate transformations" block. The definition of the t-frame and the b-frame were given in Section 4.1. The origin of the b-frame (X_b, Y_b, Z_b) is coincident with the origin of the t frame but there is a rotational transformation between the two frames represented by the 3x3 rotation matrix $\mathbf{C}_t^b$. Both coordinate systems rotate with the rate table and the rotation matrix $\mathbf{C}_t^b$ is constant. According to this definition, it is observed that the tangential velocity V_t and tangential acceleration a_t are always in $+Y_t$ direction and the centripetal acceleration a_c is always in $-X_t$ direction. By using this information and the associated rotation matrices between these coordinate systems, we can compute the accelerations and the rotational velocity experienced by the IMU, given the actual motion of the rate table. Therefore, we can generate the IMU measurements by first defining an angular velocity reference input profile for the rate table and then using the dynamic model of the rate table to compute the predicted motion of the table. This motion is then converted to the IMU measurements as given by equations (71),(72) and (73), V_{body}, a_{body}, w_{body} being the velocity, acceleration and rotational velocity experienced by the body, represented in body coordinates.

$$V_{body} = \mathbf{C}_t^b * \begin{bmatrix} 0 \\ V_t \\ 0 \end{bmatrix} \qquad (71)$$

59

$$a_{body} = \mathbf{C}_t^b * \begin{bmatrix} -a_c \\ a_t \\ g \end{bmatrix} \tag{72}$$

$$w_{body} = \mathbf{C}_t^b * \begin{bmatrix} 0 \\ 0 \\ \omega \end{bmatrix} \tag{73}$$

Data generated by the method explained above represent the exact motion parameters. However, inertial measurement units are subject to severeal errors such as bias, non-orthogonality of axes and random noise by nature. In order to generate a realistic simulation data, these error terms need to be added to idealized IMU measurements which were generated by predicted table motion and geometric calibration alone. Adding the IMU errors modelled by equations Section 2.1.2 to the exact motion variables, we get the final realistic IMU measurements.(eqns(74),(75)). The error parameters thruoughout this thesis are chosen to be consistent with the calibration parameters of the MicroStrain 3DM-GX1 IMU unless otherwise stated.

$$f = f_{exact} + \delta f \tag{74}$$

$$\omega = \omega_{exact} + \delta\omega \tag{75}$$

5.3   Camera Data Generation

Camera measurements are obtained by calculating the pixel coordinates of a feature point in the scene utilizing the projective camera model. $\mathbf{K}_{int}$ being the internal camera matrix, $\mathbf{R}_{ext}$ being the rotation of external matrix between the camera and the

global frame, and t_c being the position of camera in global frame, pixel coordinates of the feature point $P(X_p, Y_p, Z_p)$ is given by equation (11).

$$\begin{bmatrix} mp_x \\ mp_y \\ m \end{bmatrix} = \mathbf{K}_{int} \begin{bmatrix} \mathbf{R}_{ext} \mid t_c \end{bmatrix} \begin{bmatrix} X_p \\ Y_p \\ Z_p \\ 1 \end{bmatrix} \qquad (11)$$

The position of the camera is calculated at each step considering the error free dynamical model. At each step, the projection of the feature point on the image plane is calculated and stored in a 2xn dimensional array for future use. The average pixel error value is added as noise to simulated pixel measurements.

5.4 Simulations

This section intends to present the results of the simulation experiments carried out on the simulation environment created in MATLAB with the abovementioned data and the examined fusion algorithm. It is useful to remember the algorithms are named after the sensors used. These are *Kalman Filter-Gyroscope* (KF-G), *Extended Kalman Filter KF-Camera* (KF-C) and *Extended Kalman Filter KF – Gyro and Camera* (KF-GC). True states are also calculated using error-free sensor outputs and exact geometric calibration parameters for each experiment since they are vital for comparisons of the errors. Note that this is only possible in a simulation environment.

Root Mean Square (RMS) error is chosen as the performance criteria and calculated with the expression in Equation(76). RMS error is calculated after m number of runs of the algorithm since the noises are modelled as random variables.

61

$$e_{rms} = \sqrt{\frac{\sum_{i}^{m}(\hat{x}_i - x_i^{true})^2}{m}} \qquad (76)$$

Here, $\hat{x}$ is the estimated state and x^{true} is the true state of the system. Normalized root mean square estimation error can also be used as performance criteria (Eqn(77)). In some cases the RMS error might seem to have small values where the value of the state has small values itself. Also comparison of filter performance under several test scenarios having different ranges of observation data requires formalization for proper performance evaluation. When the observed test values collected for comparison have different ranges, using NRMS is better than using RMS. However in this study, the operating ranges for the tests are similar. Furthermore, we compare the performances of the three algorithms for each test separately. Hence we use state estimation RMS error as the performance criteria.

$$NRMS = \frac{e_{rms}}{x_{max} - x_{min}} \qquad (77)$$

We attempt to present each experiment together with its objective, results and main observations.

5.4.1 Experiment 1: Comparison of Gyroscope Output Integration and Kalman Filter

The first simulation experiment aims to picture the superiority of estimating angular position via Kalman Filter as compared to calculating it directly via simple integration form gyroscope measurements, which will be referred as *Direct Integration* (DI). DI yields increasing unbounded errors. We want to show that the

increase in estimation error will decrease by means of using a Kalman Filter. For this experiment, the system is simulated such that it experiences a constant angular velocity of 20degrees/sec for 60 seconds. Angular velocity profile input and the error free angular velocity output are given in Figure 26.

Generated gyroscope outputs are fed to the Kalman Filter as measurements and Kalman Filter is updated whenever a measurement is ready. The initial angular velocity and angular position are set to be both zero since the system is at rest at theta = 0 position when the input is applied. The state covariance matrix is initialized considering how well we know the initial conditions. Angular velocity is perfectly known at zero, however initial position is known on the order of external calibration error. For the real case, initial position covariance may be non-zero since it may not be measured.

$$\hat{x}(0\,|\,0) = \begin{bmatrix} 0 & 0 & 0 & 0 \end{bmatrix}^T \tag{78}$$

$$P(0\,|\,0) = \begin{bmatrix} 0 & 0 & 0 & \delta\theta_{init} \end{bmatrix} \tag{79}$$
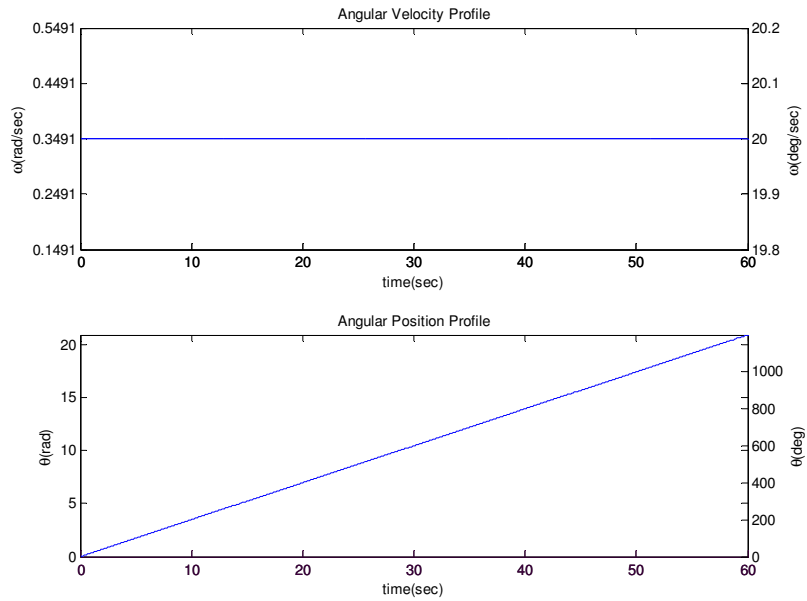
Figure 26 – Angular velocity input supplied to the dynamic system model and the
true angular position of the system for 60 seconds

KF-G and GOI performances are tested with three different gyroscopes having different random walk coefficients. These coefficients are chosen around a realistic model constructed employing the parameters of 3DM-GX1 IMU. Gyroscope model containing MicroStrain's parameters is named as g2 and has a random walk coefficient of 0.012rad/√sec. Other two gyroscopes are chosen to have random walk coefficients 0.1 and 10 times that of g2 (Table 1).

Table 1 – Gyroscope models' random walk coefficients giving a clue that g1 is better than g2, and g2 is better than g3.

random walk coefficient	Gyroscope Model 1 g1	Gyroscope Model 2 g2	Gyroscope Model 3 g3
rw	0.0012	0.012	0.12

Unbounded RMS error is demonstrated in Figure 27 for KF-G and GOI. From Figure 27-(a) and (b), it can be deducted that RMS error increases with increasing random walk coefficient for both algorithms. However, the advantage of using a Kalman Filter can be observed by comparing the y-axes values in the graphs. Final RMS values after 50 Monte-Carlo runs of 60 seconds, are gathered in Table 2.

Figure 27 – RMS error of angular position under two techniques using three different gyroscopes. (a)Kalman Filter KF-G yields 0.013 radian RMS error with the worst gyro (g3). (b) Direct calculation of angular position from the output of the gyroscope yields an RMS error of 0.025radians with the best gyro (g1) which is worst than KF-G/g3. (c) comparatively illustrates the error of KF-G and DI for (g2).
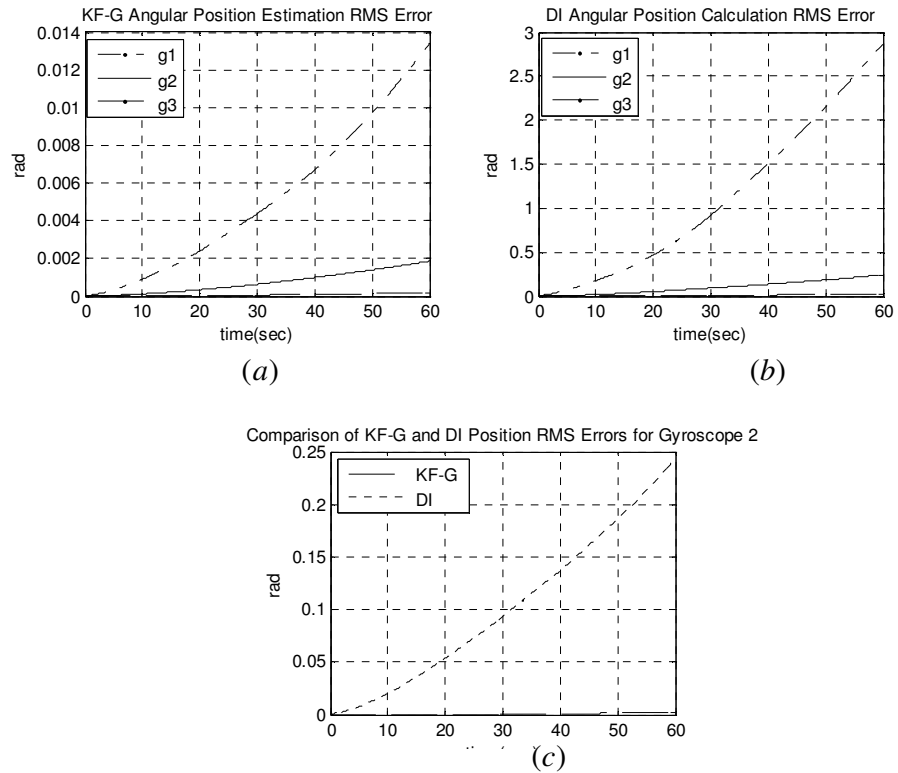
66

Table 2- Final RMS values of angular position error for KF-G and DI after 60 seconds.

	KF-G	DI
g1/drift = 0.0012	0.000193	2.8
MicroStrain 3DM-GX1 g2/drift = 0.012	0.0018	0.24
g3/drift = 0.12	0.013	0.025

5.4.2 Experiment 2: Comparison of KF-G, KF-C and KF-GC, Constant Angular Velocity

This experiment aims to support the main proposed idea of this thesis. Using a simplified set-up, we will compare the root mean square (RMS) estimation error obtained by using gyroscopes, cameras and the joint sensor configuration under nominal error characteristics. A constant angular velocity of 20 degrees per second (0.3491 rad/sec) is provided as the input to the dynamic system model for 60 seconds as in the case of Experiment 1. The angular velocity input and the true angular position are shown in Figure 26.

5.4.2.1 State estimation with gyroscope measurements: KF-G

In this experiment, we utilize the gyroscope data simulated in consistence with the specifications of MicroStrain 3DM-GX1 IMU with. Kalman Filter noise covariance value is determined according to this model.
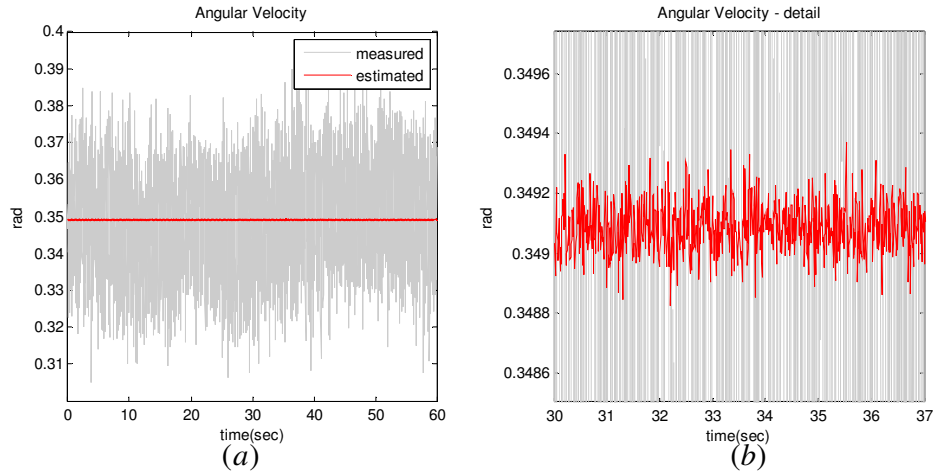
Figure 28 – (a) Angular velocity ω estimated using only gyroscope measurements in blue, with the gyroscope measurements in green and the true ω in red. (b) Detail of angular velocity estimation. Note that the estimation noise is about 100 times smaller than the measurement noise.

Linear Kalman filter structure explained in section 3.1 is utilized for this experiment. Gyroscope data is supplied at a 100Hz rate and the filter is updated when a new measurement is ready. In Figure 28 , angular velocity estimate for a single run is shown with measured and true angular velocity. Estimation noise standard deviation is 100 times smaller than the measurement noise. RMS error of estimated angular position was given in Figure 27-(a) in 5.4.1 Experiment 1.

5.4.2.2   State estimation with camera measurements: KF-C

In KF-C, we only feed camera measurements of a single point in the scene to the EKF model explained in 3.2. Camera measurements are taken 25frames/second and the filter is updated with each measurement. A pinhole model has a focal length of 20 mm and 512x512 pixels size. Ideally, internal and external calibration is perfectly known, however it is not realistic. For this experiment, the camera is assumed to

have reasonable calibration errors and pixel noise, which are likely to be obtained from the calibration algorithm used for this thesis. We assume an error of 0.45 degree standard deviation for all Euler angles between the coordinate frames which we represent by $\sigma\varphi$. All errors sum up to σtotal, total standard deviation calculated from the difference of pixel coordinates obtained from the ideal camera model and the erroneous camera model given in Table 3. σtotal, which is visualized Figure 29 for x and y directions, is utilized in measurement covariance matrix, R.

Table 3 – Nominal standard deviations on camera calibration variables.

σf	$\sigma u_0, \sigma v_0$	σskew	pixel noise	$\sigma\varphi$	σtotal
1mm	1 pixel	0.001	1 pixel	0.008rad	1.7 pixels
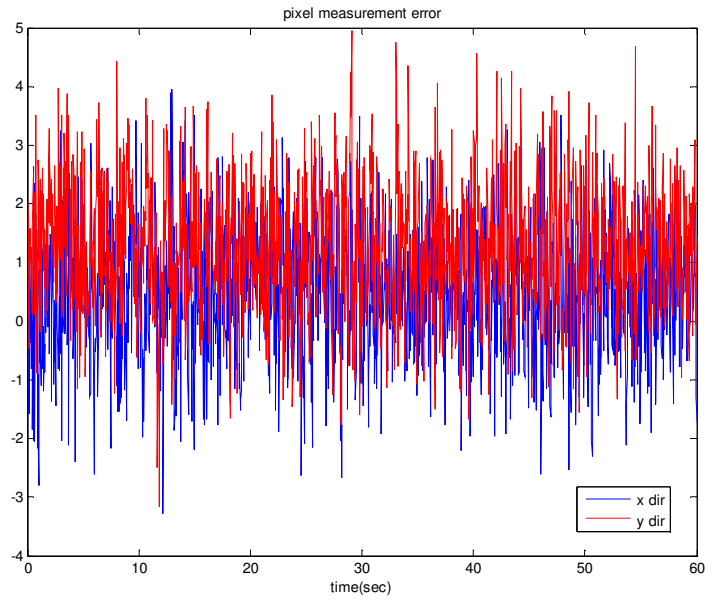
Figure 29 – Total pixel measurement error for x and y directions.
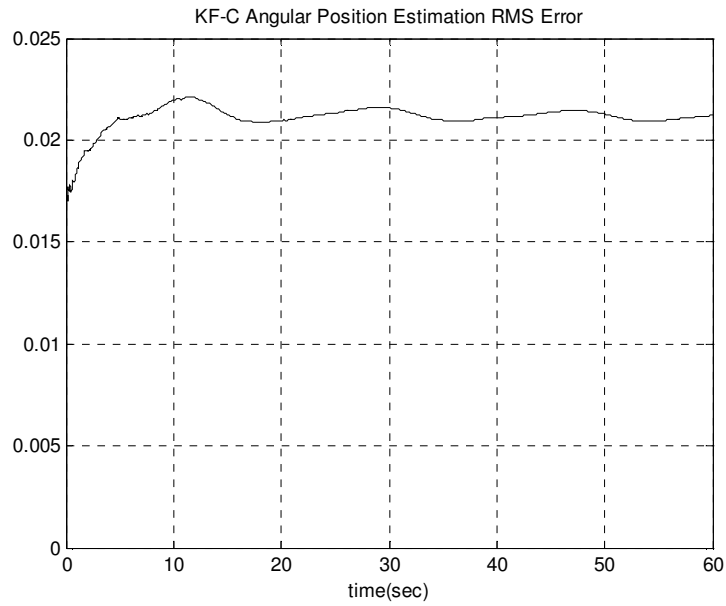
Figure 30-Angular position, θ, estimation RMS error using only camera measurements. Note that the RMS error is bounded.

The RMS error plot obtained after 50 Monte-Carlo runs show that, Extended Kalman Filter reaches to a steady state RMS value of 0.021 radians (Figure 30). This result meets our expectations of a bounded error on angular position estimate.

5.4.2.3 State estimation with joint sensor measurements: KF-GC

The aim of KF-GC of Experiment 2 is to summarize the main idea of this thesis. Both gyroscope and camera measurements are fed to Extended Kalman Filter structure and the RMS error of angular position estimation is observed. For this experiment, sensors with nominal error characteristics are used as explained in previous sub-sections 5.4.2.2and 0.
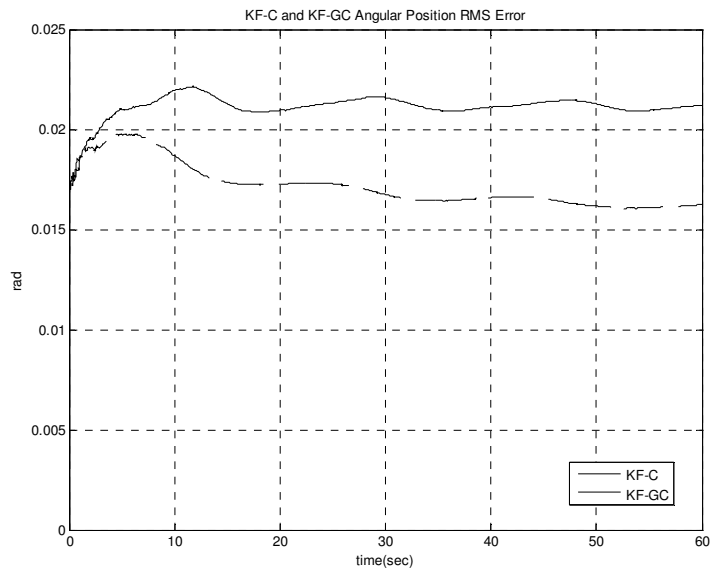
Figure 31 – RMS error of KF-C and KF-GC under nominal sensor and calibration characteristics. Note that, usage of joint sensors results in an advance in the performance.

71

It is obvious from Figure 31 that joint usage of gyroscopes and cameras provide a better performance than the sensors individually. The unbounded error growth of gyroscope is eliminated while the estimation accuracy is increased as compared to the camera alone.

5.4.3 Experiment 3: Sensitivity analysis for calibration errors

The purpose of this experiment is to analyze the performance of KF-C and KF-GC under changing calibration errors. Standard deviation of focal length, center pixel, skew coefficient and external calibration angles are varied in equal percentage steps, up and down for all variables individually. Nominal standard deviation of calibration variables used for simulations are given in Table 4.Table 5, Table 6, Table 7 and Table 8 shows the RMS errors for indicated standard deviations respectively, after rotating for 60 seconds under constant angular velocity. Columns marked with red indicate the nominal standard deviation.

Table 4 – Nominal calibration error standard deviations assumed for simulations

	σf	σ(u0,v0)	σskew	Σφ
nominal value	1 mm	1 pixel	0.0010	0.008 rad

Table 5 – RMS error of estimated angular position for options 2 and 3 under changing focal length calibration error. All other calibration errors are kept constant with previously assumed nominal values.

θ(RMS)	σf = 0.5mm	σf = 0.75mm	σf = 1mm	σf = 1.25mm	σf = 1.5mm
KF-C	0.02058	0.02113	0.02120	0.02218	0.02304
KF-G	0.01470	0.01416	0.01623	0.01658	0.01750

Table 6– RMS error of estimated angular position for options 2 and 3 under changing image center calibration error. All other calibration errors are kept constant with previously assumed nominal values.

θ(RMS)	σ(u0,v0) = 0.5px	σ(u0,v0) = 0.75px	σ(u0,v0) = 1px	σ(u0,v0) = 1.25px	σ(u0,v0) = 1.5px
KF-C	0.01920	0.020205	0.02120	0.02199	0.02220
KF-G	0.01564	0.01601	0.01623	0.01632	0.01670

Table 7- RMS error of estimated angular position for options 2 and 3 under changing skew factor calibration error. All other calibration errors are kept constant with previously assumed nominal values.

θ(RMS)	σ(u0,v0) = 0.0015	σskew = 0.00125	σskew = 0.0010	σskew = 0.00075	σskew = 0.0005
KF-C	0.0200	0.0202	0.02120	0.02245	0.02387
KF-G	0.01386	0.01533	0.01623	0.01637	0.0174

Table 8- RMS error of estimated angular position for options 2 and 3 under changing external calibration error. All other calibration errors are kept constant with previously assumed nominal values.

θ(RMS)	$\sigma\varphi$ 0.012rad	$\sigma\varphi$ =0.010rad	$\sigma\varphi$ =0.008rad	$\sigma\varphi$ =0.006	$\sigma\varphi$ =0.004
KF-C	0.02007	0.02097	0.02120	0.0239	0.02437
KF-G	0.01499	0.0158	0.01623	0.01649	0.01653

By considering the numerical values on the rows of the tables, it can be inferred that with increasing error, final RMS error of angular estimate also increases for both options. Secondly, considering columns of the tables, KF-GC performs better than KF-C for any error scheme. In Figure 32, these results are visualized. Part (a) demonstrates the performances of KF-C and KF-GC together while results of KF-GC can be seen in detail in (b). It is obvious from Figure 32-(a) that the fusion of camera and gyroscope measurements perform better for all considered conditions of

calibration errors. Apart from the individual comparison of performances, we can see that the slopes of the lines connecting final RMS error values are smaller for KF-GC. One can infer that KF-GC is more robust to increasing calibration errors. The main proposal of this thesis was to overcome the individual drawbacks of cameras and gyroscopes, which we showed with the previous experiment. Additionally, by means of this sensitivity analysis we show that KF-GC performs better and is more robust to calibration errors for all conditions considered for this thesis. This is one of the main contributions of this study.
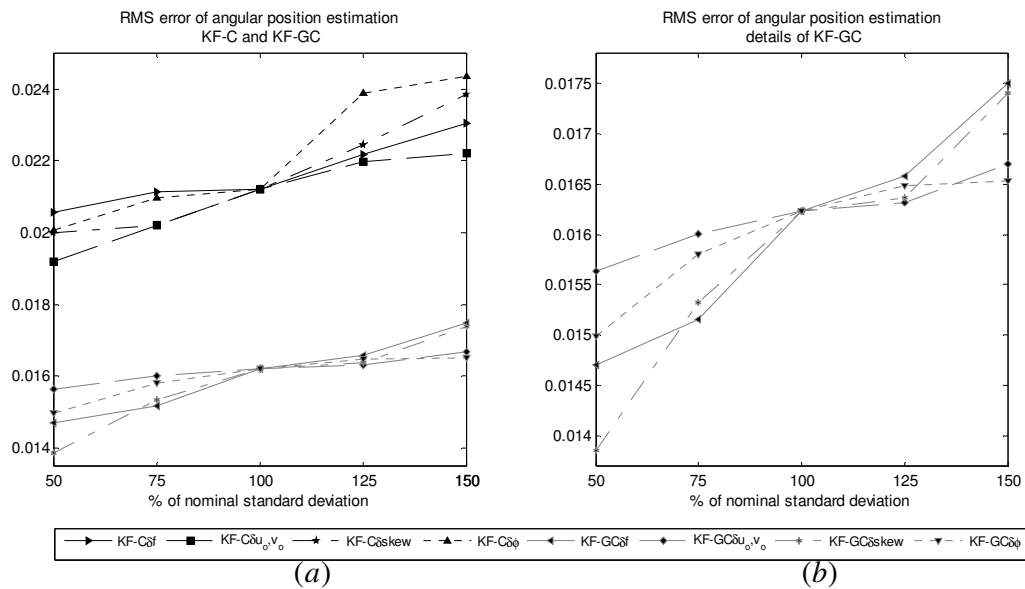

Figure 32-Angular position estimation performance (RMS error) versus percent change in nominal standard deviation of camera calibration variables.(a) demonstrates performances for KF-C and KF-GC together. In (b), performance of KF-GC can be seen in detail.

5.4.4 Experiment 4: Comparison of KF-G, KF-C and KF-GC, Ramp Angular Velocity

In this experiment, the angular position is a ramp function with an angular acceleration of 0.0175 rad/sec^2 (1 deg/sec). The angular velocity and position profile is shown in Figure 33. The performances of KF-G, KF-C and KF-GC are compared in this section. This experiment aims to observe the performance of the algorithm under ramp input.

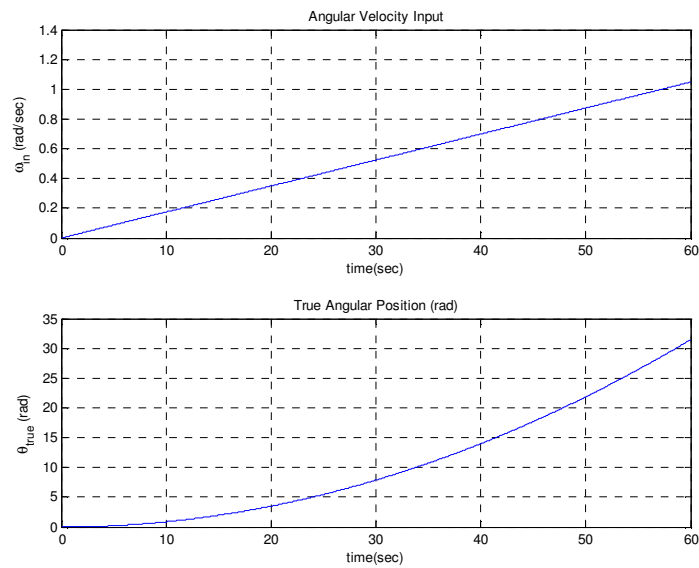Figure 33 – Angular velocity and position profiles for experiment 4.

5.4.4.1 State estimation with gyroscope measurements: KF-G

State estimation of KF-G with ramp angular input yielded the expected result of unbounded error growth. The RMS error increase is given in Figure 34. Note that the error value at second 60 is slightly larger than that of KF-G with constant angular velocity input.
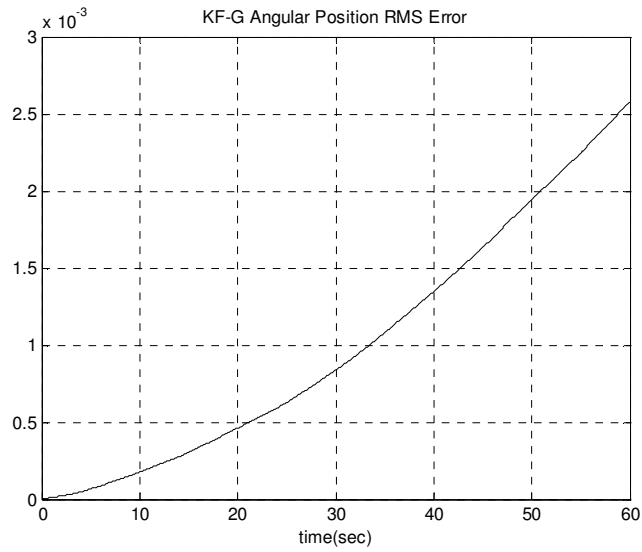
Figure 34 – KF-G angular position RMS error increases with time. The angular velocity input is a ramp function.

5.4.4.2   State estimation with camera measurements: KF-C and KF-GC

Angular position estimation error for KF-C and KF-GC under ramp angular velocity input is shown in Figure 35 comparatively. Final RMS error of KF-C is 0.019 rad where this value reduces to 0.016 radians for KF-GC. The fusion of the sensors provides the expected improvement on the RMS error.

77
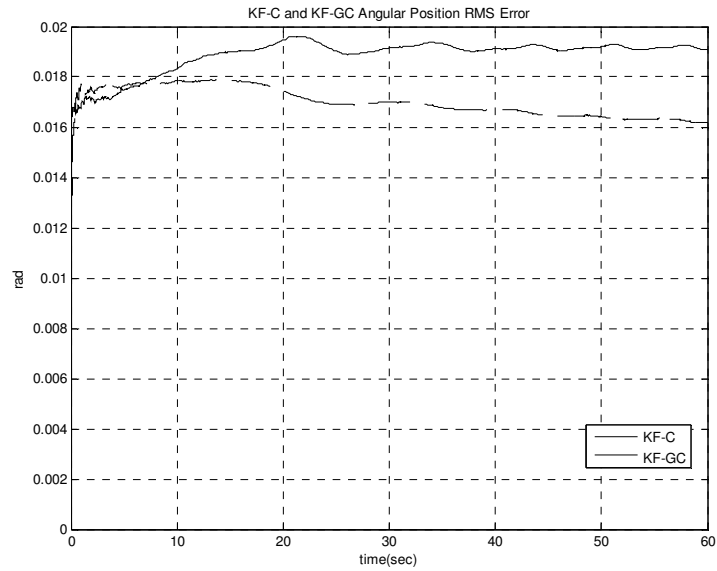
Figure 35 – KF-C and KF-GC angular position RMS error graphics. Fusion of the sensors introduces an improvement to estimation error.

5.4.5   Experiment 5: Comparison of KF-G, KF-C and KF-GC, Arbitrary Angular Velocity

In this experiment, the performance of KF-G, KF-C and KF-CG are evaluated under a varying angular velocity input profile with the plot given in Figure 36. The profile includes accelerated regions as well as constant angular velocity. The angular position estimation errors for all KF filter options are presented in this section.
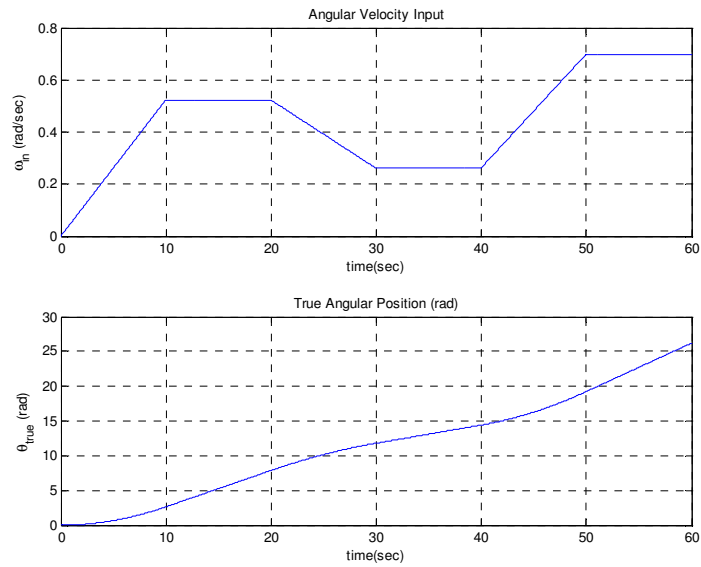
Figure 36 – Angular velocity input profile for Experiment 5 and the associated True Angular Position

Position estimation error for KF-G is unboundedly growing as Figure 37 demonstrates. The final value of the error after 60 second is 0.00185 radians which corresponds to 0.1 degrees. KF-C with arbitrary angular input has finite error characteristics while we can observe some fluctuations on the error signal. The RMS value at 60th second is around 0.0023 radians. Introducing the sensor pair to the system, KF-GC provides better estimation performance, with final simulated value of 0.016 radians. The unbounded error is eliminated.
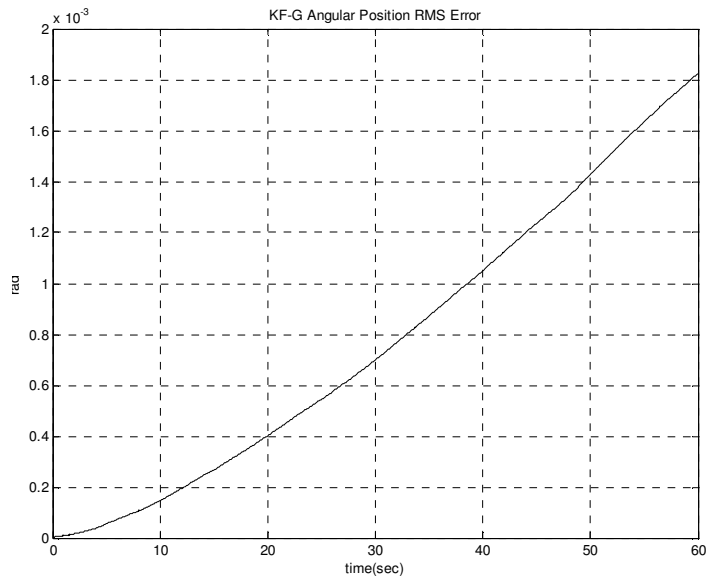
Figure 37 – Angular position RMS error of KF-G for Experiment 5
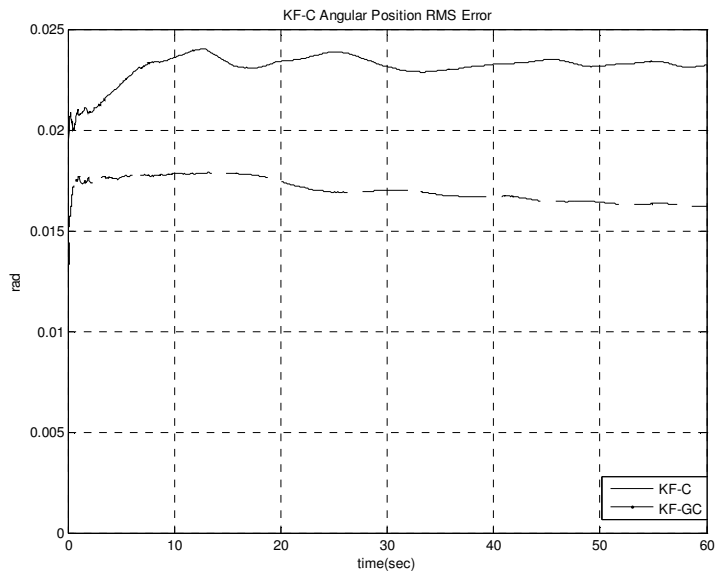
Figure 38- Angular position RMS error of KF-C and KF-GC for Experiment 5.

5.4.6 Experiment 5: Long term comparison of KF-G, KF-C, KF-GC

The aim of this experiment is to observe the behaviors of the proposed algorithms in short time and long time. The experiment lasts for 200 seconds for a constant angular velocity input.

It has been shown that the angular position estimation error for KF-G grows exponentially with time. Although unbounded, the short term performance of KF-G is better than the both camera alone and the fusion of the two sensors. In Figure 39, the estimation performances of three sensor configurations are demonstrated together. We can observe that till 100th second, KF-G performs better than the fusion of the sensors and till 123rd second, it performs better than the camera alone. We can deduce that the estimation with gyroscope only is more accurate in short time but the stable estimation error of KF-C and KF-GC are more reliable when the run time is longer.
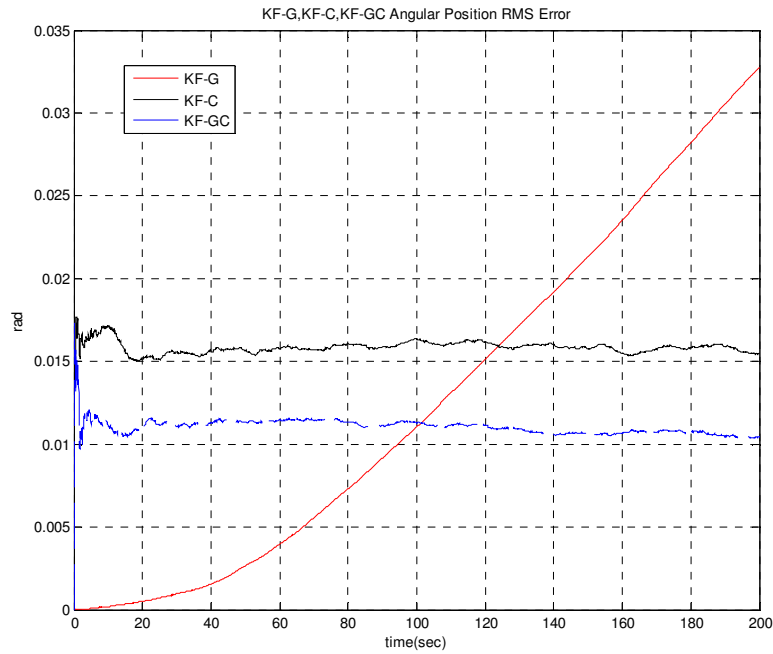
Figure 39 – Comparison of KF-G, KF-C and KF-GC angular position RMS error for duration of 200 seconds. Note that the short-term performance of KF-G is better than KF-C and KF-GC. KF-GC outperforms KF-G after 100 seconds and KF-C outperforms KF-G after 123 seconds.

5.4.7   Experiment 6: Comparison of KF and IKF

We have mentioned that angular position integration is running outside the Indirect Kalman Filter structure. The camera measurements are used to correct the integration outputs. In this simulation experiment we compare the performance of KF-GC and IKF.
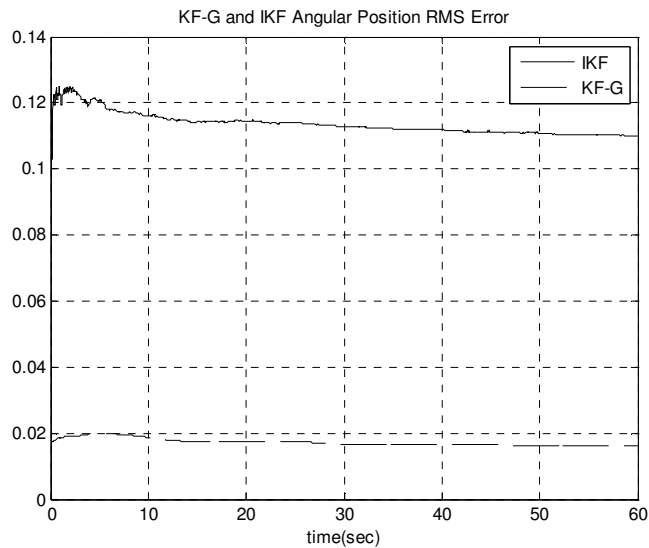
Figure 40- KF-G and IKF angular position estimation RMS error comparison.

The error characteristics of the algorithms are presented in Figure 40. The unbounded error caused by integration is avoided. However, the error level is above the error level obtained by KF-G. The inclusion of the accurate dynamical model of the system in KF-GC algorithm provides a better body state estimation error. This result is discussed in section 5.5

5.5   Simulation Results: Discussion

In this section, the performance of the proposed fusion approach is observed in a simulation environment under predefined experimental conditions and realistic error assumptions. The Root Mean Square (RMS) value of state estimation error is considered as the performance criteria. Experiments are carried out under constant, ramp and arbitrary angular velocity inputs and perfectly known initial state assumption.

83

Initially, the effect of using a Kalman Filter structure to estimate angular velocity and angular position is compared with the Direct Integration approach, where angular position is calculated by direct integration of gyroscope measurements. The RMS performance measure on angular velocity estimate improves significantly, but the unbounded increase in angular position estimate cannot be eliminated. However the increase in error is smaller than direct integration which enables us to the system for a slightly longer time.

Estimating with camera-based KF-C structure is considered as the second step for our simulations. The estimation error is bounded since the position measurement based on a fixed landmark is absolute. However for short time, the RMS error of KF-G is still smaller.

The fusion of the sensors eliminate unbounded error characteristic of gyroscopes while improving the performance of stand-alone camera based KF-C. For any angular position input, whether it is constant, ramp or an arbitrary input, the ordering of the performance does not change.

The sensitivity analysis shows that the fusion of the sensors introduces robustness to calibration errors. The estimation performance of KF-GC is better than that of KF-C for any of the considered calibration error value. Moreover, the slope of performance with respect to parameter variations is reduced with the fusion, indicating a improving robustness to parameter variations.

The need for an accurate dynamic system model is eliminated in the case of Indirect Kalman Filter. However, the angular velocity estimate is directly obtained from the gyroscope measurements and the noise level is equal to that of the gyroscope, namely higher than the Direct Kalman Filter case. Also the angular position estimation error is lower when the system dynamical equations are included in the system with the Direct Kalman Filter Approach. Although it has higher performance, direct filtering requires dynamical system modelling which can be complicated in

many real systems. With lower number of states, run time of IKF is smaller. This may be the main reason IKF is preferred in Inertial Navigation Systems (INS). Another advantage of IKF is that navigation equations keep providing outputs even if the Kalman Filter block fails to operate. Depending on the demands of the system, the suitable algorithm could be chosen considering the advantages and disadvantages of each algorithm.

CHAPTER 6

HARDWARE EXPERIMENTS

Computer simulations are important in the sense that we can test if the proposed method yields the expected results in controlled conditions. Also, ground truth is readily available in a simulation experiment. However, one should be careful with simulation experiments as there may be unexpected/unmodelled influence factors that can only be seen by real hardware experiments. Hence these become crucial to investigate the performance of the investigated approaches in an imperfect environment. With these motivations, we have also considered real hardware experiments and the results of these are presented in this chapter.

6.1   Experiment Set-up

The experimental set-up consists of a rate table, an IMU, a webcam, 2 laptops and a power supply to feed the rate table.

The IMU used for the experiments is MicroStrain's 3DM-GX1 which has been characterized through several tests. The camera is a commercial webcam by Apache. The rate table is a product of IMAR Navigation Company. The rate table is driven by a 24 V power supply. The communication is via RS232 serial port and a user interface supplied by the manufacturer. However, to fully control the input commands timing; we wrote our own scripts which are sent to the table from the communication port. A picture of the experimental set-up is illustrated in Figure 41.
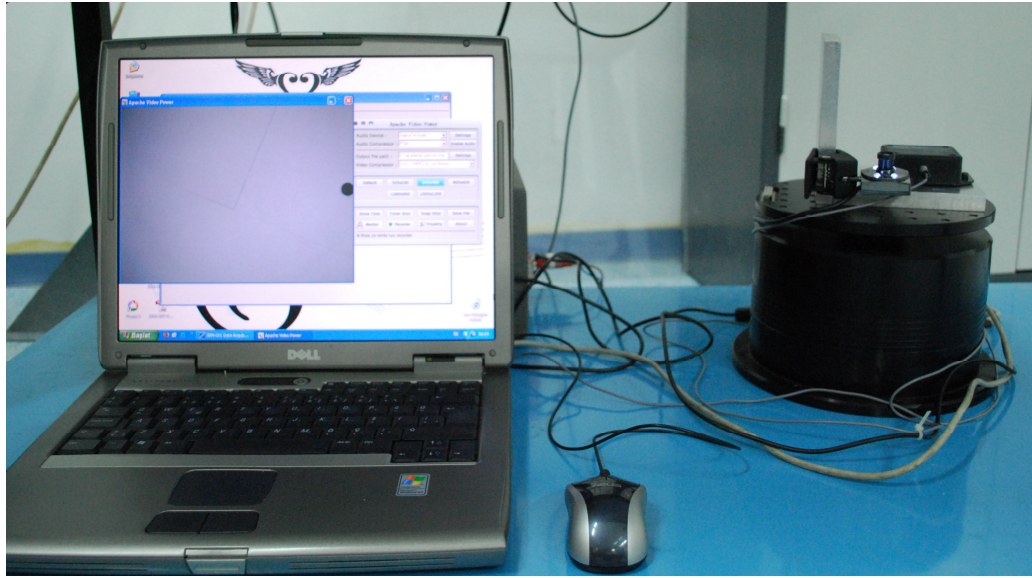
Figure 41 – Experimental set-up. The sensor pair is seen on the rate table.

6.2 IMU Data Collection

The IMU has an RS232 connector for communication and an electricity network connection plug to meet the power demand. It is possible to use the graphical user interface supplied by the manufacturer or write a program to collect the raw data as in the case of this study. The raw data is collected and then converted to physical units before running the body state estimation algorithm. The parameters necessary for this operation has been explained in Section 2.1.3.
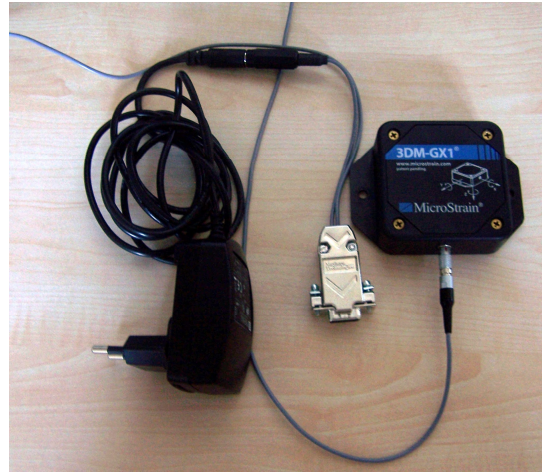
Figure 42 – Inertial measurement unit shown with connection cables.

6.3   Camera Data Collection

The camera used in this study is a commercial webcam of Apache. The camera is connected to the laptop with a USB port and it draws the necessary power from the USB port of the computer. Camera images are 480 pixels by 640 pixels and are captured by using the commercial program Apache Video Power with a rate of 30 frames/sec and stored for processing.

Figure 43 – Apache webcam and the USB connector

IMU and camera are mounted on the rate table via a mechanical interface (Figure 44). Camera optical axes points upwards. External calibration is performed with the calibration rig observed in the scene. After external calibration, a black circular point with known coordinates is introduced to the scene with a white background. The center of the point is to be used as the measurement from the camera.
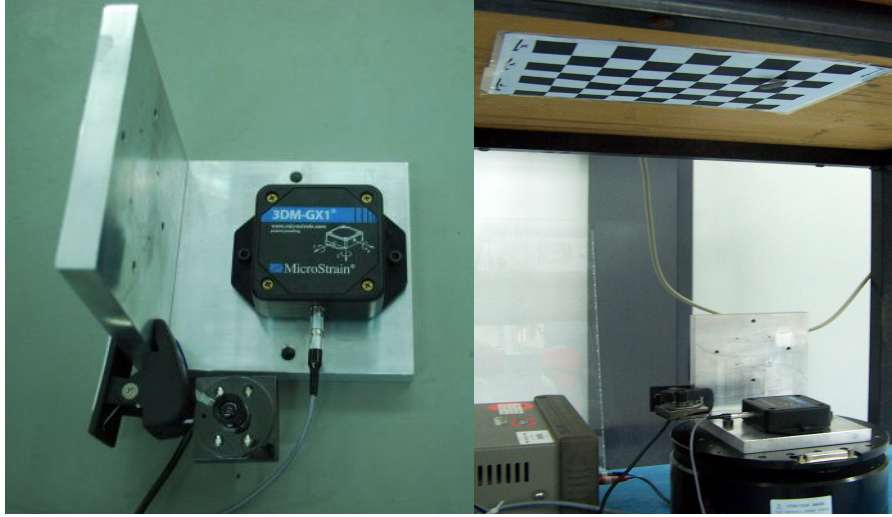
Figure 44 – IMU and camera are mounted on the rate table with a mechanical interface. Camera optical axes points upwards. External calibration is performed with the calibration rig seen in picture on the right.

The reason for choosing a circular black point with a white background is to simplify the image processing part. The center of the point is our main interest since we want to calculate the 2D projection on the image plane. The *center of mass* of the black point is given by equations(80), (81) and(82) after the image frames are binarized. The colored image and the binarized image can be seen in Figure 45. The center of mass of each image is calculated and stored in an array.

$$A = \sum_{j}^{n} \sum_{i}^{m} b_{ij} \tag{80}$$

$$\overline{x} = \frac{\sum_{y}^{n} \sum_{x}^{m} x b_{xy}}{A}, \ \overline{y} = \frac{\sum_{y}^{n} \sum_{x}^{m} j b_{xy}}{A} \tag{81}$$

$$b_{ij} = \begin{cases} 1 & \textit{for points on the object} \\ 0 & \textit{for points on background} \end{cases} \tag{82}$$
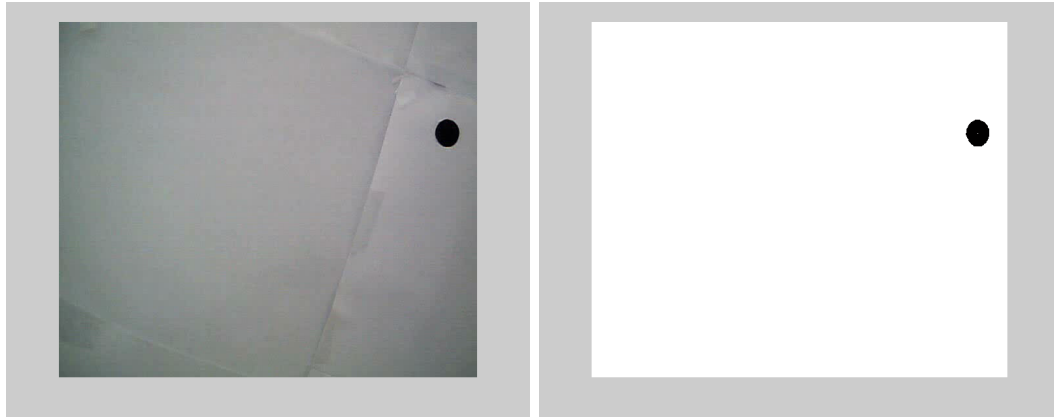

Figure 45 – An image of the black point in the scene captured from the camera. The binarized image is displayed on the right.

6.4 Data Synchronization

Data is straight forward in simulation since the data is artificial. However, in hardware experiments, synchronization is an important issue. Data sampling rates are mostly different in sensor fusion applications. The sensors used in this study have sampling rates of 100Hz for the gyroscope and 30frames/second for the camera. Neither the time stamps of the sensors coincide nor can they be triggered at the same time. The start point of the motion can be detected on the outputs of the sensors and time stamped as 0. The gyroscopes have their own time tags starting from the transferred data frame initially. The same motion is detected in the camera frame. Starting from 0, the time stamp of each frame is marked with intervals of 0.033 seconds.
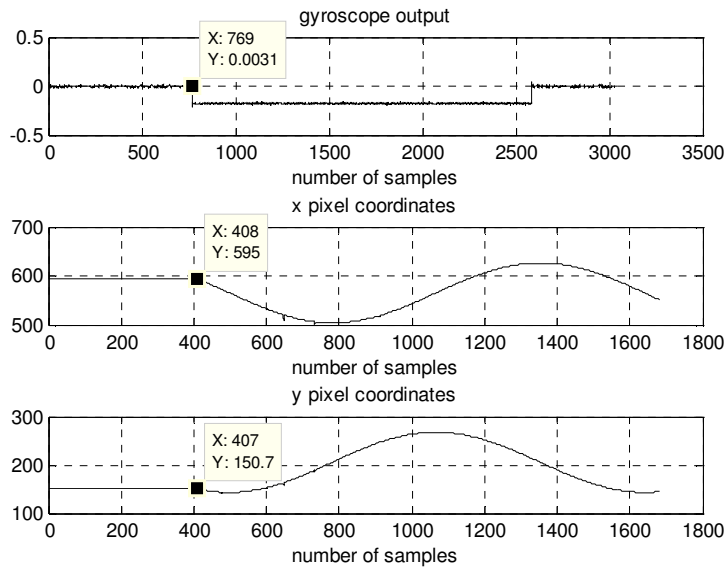
Figure 46 – Gyroscope output and pixel coordinates of the object in the scene. The input is constant angular velocity. Data points after collection of experiment data can be distinguished. The initial data point is marked.

Camera data points are interpolated using linear interpolation to calculate the pixel values at gyroscope sampling times. Finally we have the measurements of both sensors at any time stamp. This distinctive motion is used synchronization before inputting the actual angular velocity profile.

6.5   Experiments

Hardware experiments are classified considering the angular velocity command supplied to the rate table. In consistent with the simulation experiments, constant angular velocity and ramp angular velocity inputs are applied to the system.

6.5.1 Experiment 1: Comparison of KF-G, KF-C, KF-GC, Constant Angular Velocity

This experiment is the hardware equivalent of simulation experiment 1. The input is constant angular velocity. The RMS errors of angular position estimations are presented.

6.5.1.1 State estimation with gyroscope measurements

Data collected from IMU vertical axes gyroscope, is used as measurements to the Kalman Filter in this experiment. Angular position estimation RMS error is increasing unboundedly as foreseen form the simulation experiment results.
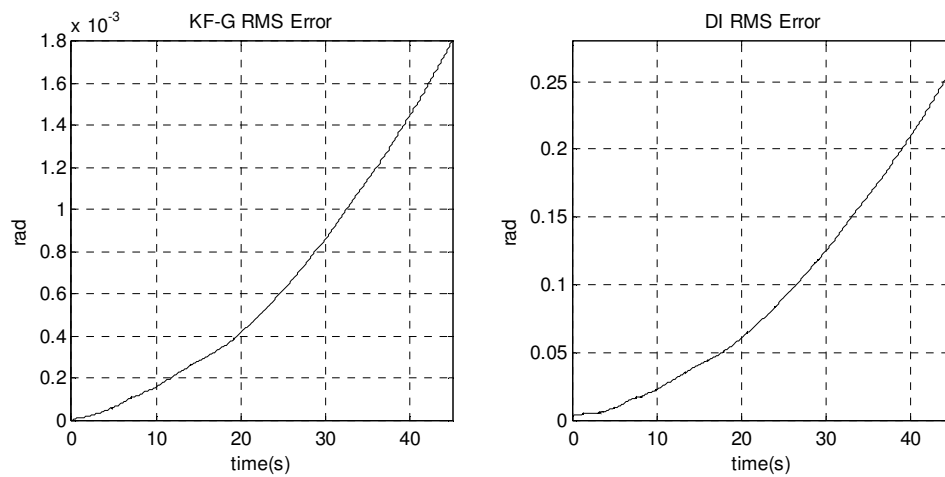

Figure 47 – Angular position esitmation RMS error of KF-G with real set-up. Note that the error increases with time. DI angular position calculation error is also demonstrated.

6.5.1.2   State estimation with camera measurements

Image frames from Apache webcam is collected by a laptop in 25frames/sec. After collection of all frames, the center of mass of the object in the scene is calculated offline before running the algorithm. The RMS error in angular velocity reaches to a steady state as expected.

Figure 48 - Angular position esitmation RMS error with KF-C with real set-up. Note that the error is bounded.

6.5.1.3   State estimation with joint gyroscope and camera measurements

Both sensor measurements are fed to the Extended Kalman Filter which is updated whenever a measurement is ready, whether from the gyroscope or the camera. Angular position RMS error reaches to a steady state smaller than KF-C, eliminating the unbounded error increase in KF-G.
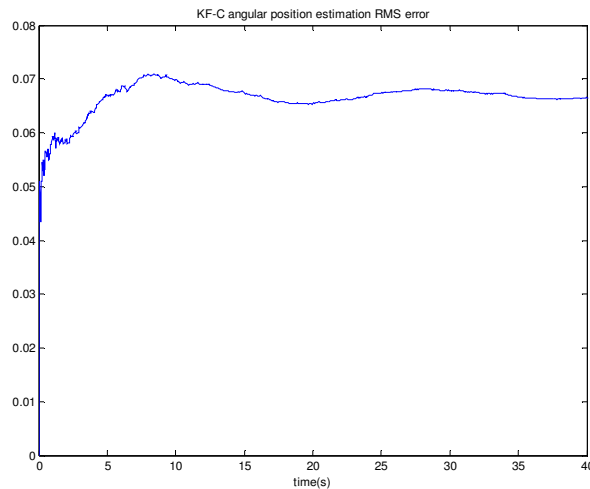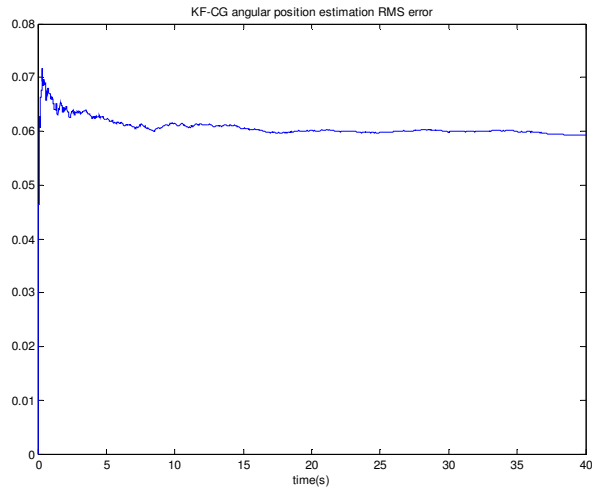
Figure 49 - Angular position esitmation RMS error with KF-CG with real set-up.
Note that the error is bounded and smaller than the RMS error obtained with KF-C.

6.5.2 Experiment 2: Comparison of KF-G, KF-C, KF-GC, Ramp Angular Velocity

The input profile for experiment 2 is ramp angular velocity with angular acceleration of 0.05 deg/s^2. Gyroscope and camera outputs after data synchronization are given in Figure 50 . Camera x-pixel and y-pixel measurements are demonstrated separately. We evaluate the DI outputs as well as KF outputs. True and DI angular position profiles are displayed on the same graph illustrating the deviation of DI output from the true angular position value (Figure 51-(a)). Figure 51-(a) shows the RMS error of DI angular position calculation while KF-G estimation is demonstrated in Figure 52.
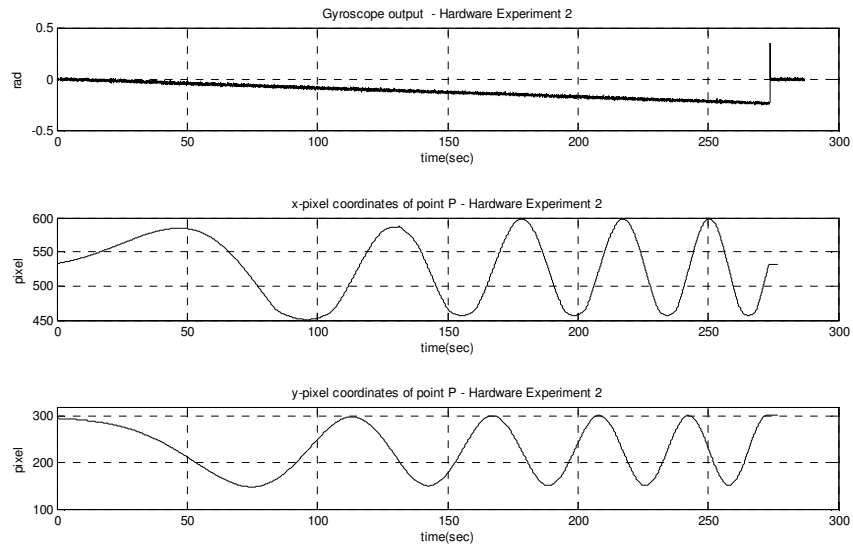
Figure 50 – Synchronized sensor outputs of experiment 2. Gyroscope ramp output, camera x-pixel position of point P and camera y-pixel position of point P.
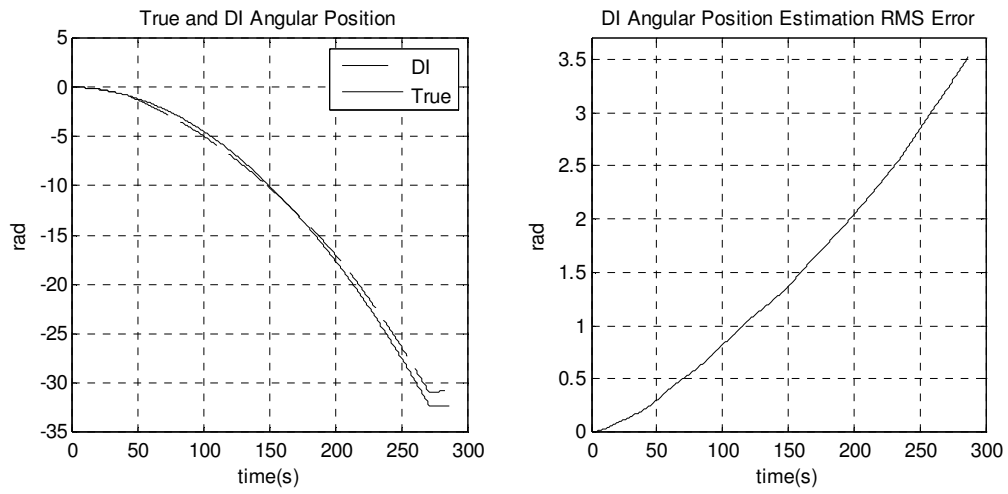
Figure 51 – (a) True and DI angular position profile and (b) DI angular position error.
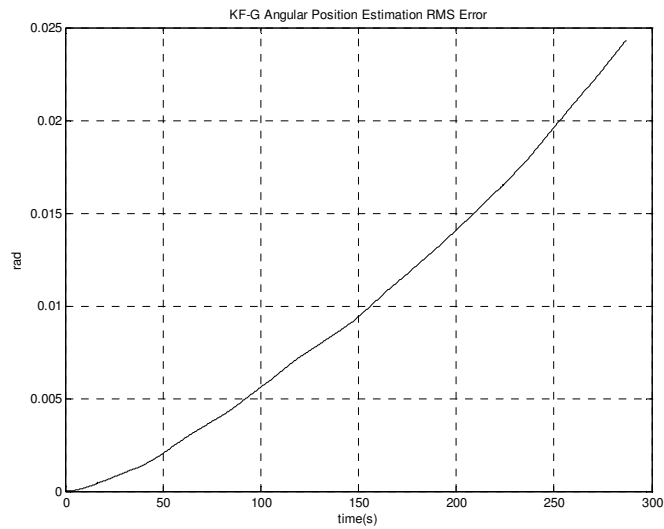
Figure 52 – KF-G angular position RMS error of experiment 2.

For ramp angular velocity input, fusion of sensors develops the estimation performance a significant level. Figure 53 clearly illustrates this improvement by showing the angular position estimation RMS error on the same graph.
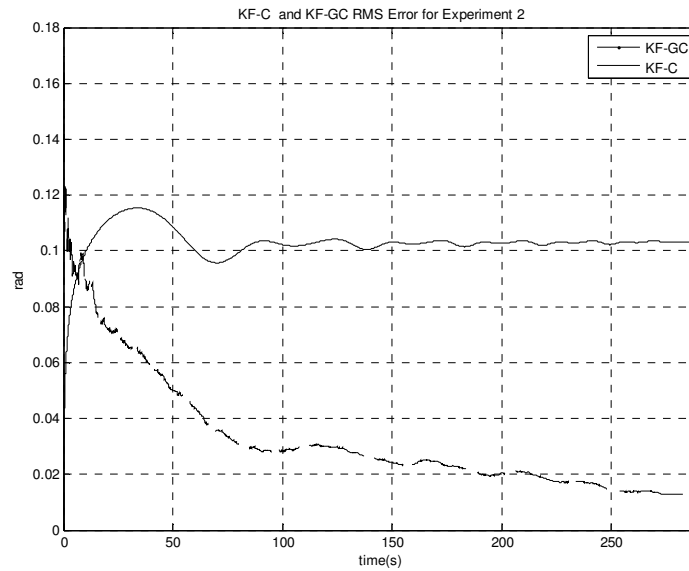
Figure 53 – KF-C and KF-GC Angular position RMS error for hardware experiment 2.

6.5.3 Experiment 3: Comparison of KF-G, KF-C, KF-GC, Arbitrary Angular Velocity

In this experiment, we evaluate the performance of the proposed algorithms under variable angular velocity input. The gyroscope output collected during the experiment is given in Figure 54.
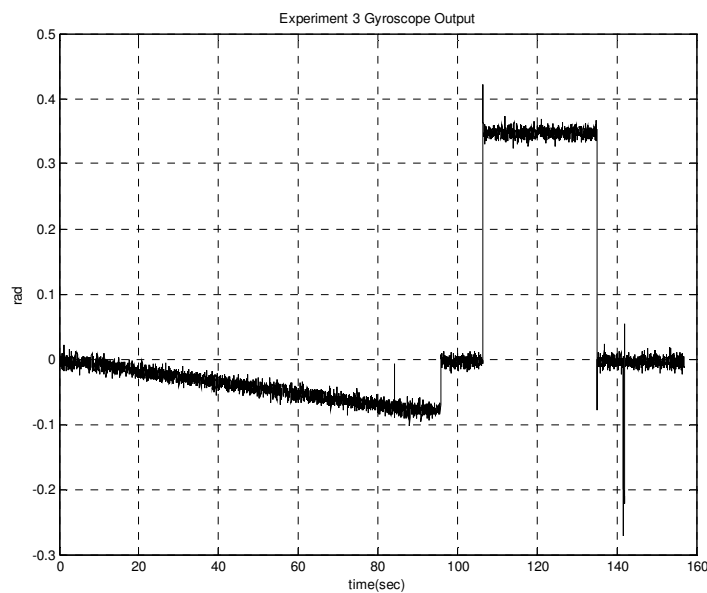
Figure 54 – Experiment 3 gyroscope output.

The angular position estimation error of KF-G is given in Figure 55 where the unbounded error increase can be observed. The error level is similar to the error level obtained in simulation experiments. We can observe the expected behavior for KF-C and KF-GC case where the error graph is provided in Figure 56. The

estimation error is bounded and the performance of KF-GC is improved with respect to KF-C.
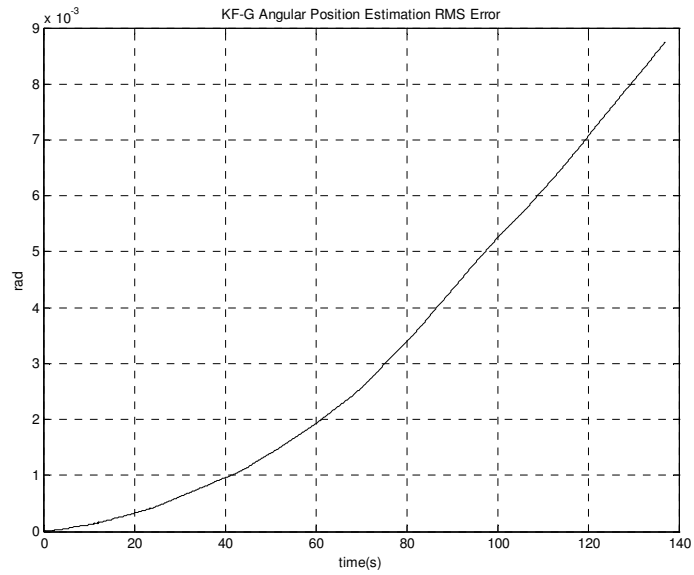
Figure 55 – Experiment 3 KF-G angular position RMS error
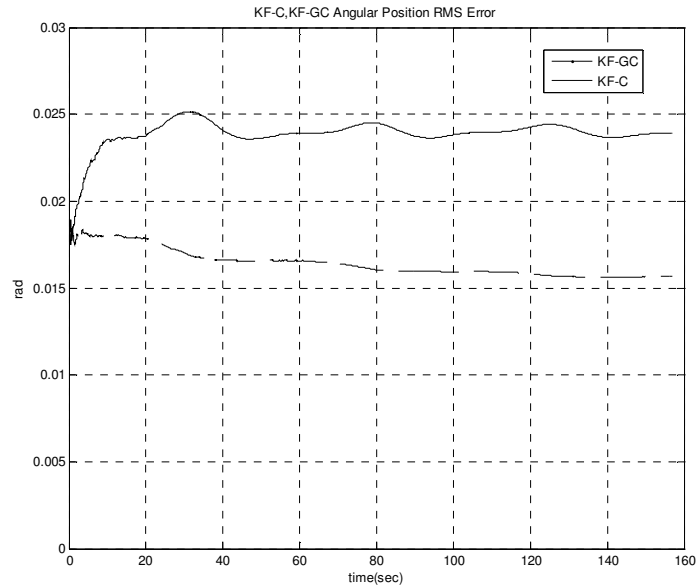
Figure 56 – KF-C and KF-GC angular position estimation RMS error.

6.6   Experiment Results: Discussion

Hardware experiments are conducted in laboratory environment in a controlled set-up which is explained in Section 5.1. The objective of hardware experiments is to see if the simulation results can be verified.

The RMS errors of angular position estimation are calculated for KF-G, KF-C and KF-GC under constant, ramp and arbitrary angular velocity excitation. Performance development arising form the use of dynamical modelling and an optimal state estimator is clearly indicated with the given DI performance in comparison with KF-G. It is shown that the fusion of the sensors outperform the use of the sensors individually. This result is in consistence with the results obtained in simulations.

CHAPTER 7

CONCLUSION

7.1 Discussion of Results

In this thesis, we investigated the benefits of fusion of IMU and Camera under the Kalman Filtering framework. This has been done comparatively both as simulation and real hardware experiments. The calibrations of both sensor types are studied as well as the sensor fusion strategies including Direct and Indirect Kalman Filter structures. Although still not bounded, the divergent error growth of DI can be significantly reduced by single sensor Kalman based estimation (KF-G algorithm). This algorithm is not suitable for long term estimation but provides accurate results in short time. On the other hand, bounded error can be obtained by direct measurement of the camera sensor or by Kalman estimation based on stand-alone camera measurements (KF-C algorithm). However, the camera sensor measurements are noisy and the sampling rate is much lower than an IMU. Sensor fusion based on Direct Extended Kalman Filter (KF-GC algorithm) benefits from an accurate dynamical system model and successfully integrates the advantages of each sensor. The unbounded error growth of stand-alone IMU based estimation is avoided and KF-GC also outperforms KF-C in terms of estimation RMS error. Moreover, the output of the sensor fusion has the high sampling rate of the IMU. This result remains valid for different angular velocity input profiles. The system is simulated for varying calibration errors. It is shown through the sensitivity analysis that KF-GC is more robust to calibration errors.

We have also compared the angular position estimation performance with the Indirect Kalman Filter (IKF) with that of Direct Form KF-GC. The results show that the true angular position profile can be tracked with slightly higher but still bounded error characteristics. Since IKF formulation does not make use of a dynamic system model, it enables the algorithm developer to use the same structure on the platform even if the platform dynamical model is unknown or has changed. This may be an advantage in some applications and the complexity is reduced by sacrificing the accuracy to some extend. It is also possible to obtain position and velocity information for a limited time with IKF even if the Kalman Filter block fails to operate. Direct form would be a good choice when an accurate the dynamical system model is present and the computational capability is high.

Our promising simulation results are also validated with real hardware experiments on a controlled rotation rate-table. It has been shown that the real hardware experiments yielded the simulation suggested results, resulting in concrete and reliable observations. We can confidently conclude at this point that the fusion of low-cost inertial sensors with low cost cameras represent a promising direction to design high performance body state estimation mechanisms by exploiting the advantages of each particular sensor. We also observe that the Kalman Filtering framework is a successful methodology to realize this potential.

7.2 Future Work

One of the objectives of this work is was show that a high performance body state estimation is possible with the fusion of low-cost off-the-shelf IMUs and Cameras. A comparative study can also answer the following question: Can a low-cost IMU - camera pair equal or exceed the performance of a high-cost IMU possibly based on a different sensing technology? Mounting a more sophisticated IMU to the proposed experimental set-up, the performances of the pair and the single IMU can be easily

evaluated. The extension of the proposed algorithm and the experimental set-up to higher DOF system is an interesting and promising subject in conjunction with the study in this thesis.

We implemented Direct and Indirect Kalman Filters in this study with linearization when necessary (in the form of Extended Kalman Filter) Another interesting extension would be a comparative study considering the Unscented Kalman Filters and/or Particle Filters which are usually better estimators for non-linear systems. For a more complex experimental set-up with a complex dynamical model, the non-linearities may cause the Taylor Series based direct linearization and hence the Extended Kalman Filter to diverge. In this case, Unscented Transform may be a better alternative. Particle Filters can handle process and measurement noises which are not Gaussian and may also be a feasible possibility for some applications despite the high computational load involved This non-Gaussian assumption is mostly more realistic since noises of real systems may not be modelled with Gaussian distribution. It is important to judge the benefits and the disadvantages considering the expected performance and the attributes of the dynamical system.

REFERENCES

[1] "IEEE Standard Definition of Navigation Aid Terms" ,*Guidance and Control Systems Panel of IEEE Aerospace and Electronics Society*, 1983, USA

[2] Engman A, "Study of Gyro and Differential Wheelspeeds for and Vehicle Navigation" , Ms.Thesis, Royal Institute of Technology, 2006, Sweden

[3] Elkaim G. H., Lizarraga M. and Pederseny L., "Comparison of Low-Cost GPS/INS Sensors for Autonomous Vehicle Applications", *IEEE/ION Position, Location and Navigation Symposium,* 2008.,pp. 1133-1144.

[4] Bingbing L, Martin A. and Ibañez-Guzman J., "Multi-aided Inertial Navigation for Ground Vehicles in Outdoor Uneven Environments", *Proceedings, IEEE International Conference on Robotics and Automation*, Barcelona, Spain, April 2005.

[5] Lazarus S.B. et al, "Vehicle Localization Using Sensors Data Fusion Via Integration of Covariance Intersection and Interval Analysis", *IEEE Sensors Journal*, Vol.7 No.9, September 2007.

[6] Park M, "Error Analysis and Stochastic Modeling of MEMS based Inertial Sensors for Land Vehicle Navigation Applications" Ms.Thesis, University of Calgary, April 2004.

[7] Green W E. and Oh P. Y., "Autonomous Hovering of a Fixed-Wing Micro Air Vehicle" , *IEEE International Conference on Robotics and Automation(ICRA)*, pp. 2164-2169, Orlando , May 2006

[8] Soon J.J. and Darren L., "Automation of Small UAVs Using a Low Cost MEMS Sensor and Embedded Computing Platform", Crossbow Technology Inc.

[9] Goehl D. and Sachs D., "Motion Sensors Gaining Inertia with Popular Consumer Electronics", White Paper, IvenSense Inc., 2007.

[10] Diel D., "Stochastic constraints for vision aided inertial navigation", Ms.Thesis Massachusetts Institute of Technology, Jan.2005

[11] Chroust S.G, Vincze M, "Fusion of vision and inertial data for motion and structure estimation", *Journal of Robotic Systems*, 2004

[12] Mukai T, Ohnishi N., "The Recovery of Object Shape and Camera Motion Using a Sensing System with a Video Camera and a Gyro Sensor", *IEEE International Conference on Computer Vision,*1999

[13] You S., Neumann U., Azuma R., "Hybrid inertial and vision tracking for augmented reality registiration", *IEEE Virtual Reailty Conference,* 1999

[14] Aron M. , Simon G., Berger M.O., "Use of inertial sensors to support visual tracking", *Computer Animation and Virtual World,*31.10.2006

[15] Titterton D.H. and Weston J.L, *Strapdown Inertial Navigation Technology*, The American Institute of Aeronautics and Astronautics, USA, 2004.

[16] Trucco, Verri A. ,Introductory Techniques for 3D computer vision, Prentice Hall, 1998

[17] Tsai R.Y., "A Versatile Camera Calibratio Tehcnique for High- Accuracy 3D Machine Vision Metrology Using Off-The-Shelf TV Cameras and Lenses" , *IEEE Journal of Robotics and Automation*, Vol. RA-3 No:4, August 1987

[18] Heikkila J, Silven O, "A Four-step Camra Calibration Procedure with Implicit Image Correction" , *IEEE Computer Vision and Pattern Recognition Conference,*1997

[19] Zhang Z., "Flexible Camera Calibration by Viewing a Plane From Unknown Orientations", *IEEE International Conference on Computer Vision*, September 1999

[20] Camera Calibration Toolbox For Matlab, "www.vision.caltech.edu/bouguetj/calib_doc", (Accessed 19 August,2009)

[21] Smith M.J., Qtaishat K.S., Park D.W.G, Jamieson A., "IMU and Digital Aerial Camera Misalignment Calibration", *International Calibration and Orientation Workshop*, January 2006

[22] Alves J., Lobo J., Dias J., "Camera-Inertial Sensor Modelling Alignment for Visual Navigation", *International Conference on Advanced Robotics*, July 2003

[23] Lobo J., Dias J. , "Relative Pose Calibration Between Visual and Inertial Sensors", *Workshop on Integration of Vision and Inertial Sensors* , ICRA 2005-InerVis,

[24] Inertial Vision (InerVis) Toolbox for MATLAB ,

"http://www2.deec.uc.pt/~jlobo/InerVis_WebIndex/InerVis_Toolbox.html", (Accessed 19 August 2009)

[25] Mirzaei A.M., Roumeliotis S., "A Kalman Filter-based Algorithm for IMU-Camera Calibration", *IEEE International Conference on Intelligent Robots and Systems,* November 2007

[26] Roumeliotis S.I., Sukhatme G.S., Bekey G.A., "Circumventing Dynamical Modeling: Evaluation of the Error-State Kalman Filter applied to Mobile Robot Localization", *IEEE International Conference on Robotics and Automation*, May 1999

[27] Blomster J, "Orientation estimation combining vision and gyro measurements", Ms.Thesis KTH Electrical Engineering, June 2006

[28] Klein G., Drummond T., "Tightly integrated sensor fusion for robust visual tracking", *British Machine Vision Conference,*2002

[29] Strelow D, "Motion estimation from image and inertial measurements", PhD Thesis Carnegie Mellon University, November 2004

[30] Sönmez T.and Aslan G.," Development of a Software Testbed for Integrated Navigation Systems" (In Turkish), *IEEE 15th Signal Processing and Communications Applications*, SIU2007, 2007. Eskişehir, Turkey

[31] Aslan G.,Saranli A., "Characterization and Calibration of MEMS Inertial Measurement Units ", *16th European Signal Processing Conference,* Aug. 2008

[32] Park M, "Error Analysis and Stochastic Modeling of MEMS based Inertial Sensors for Land Vehicle Navigation Applications" Ms.Thesis, University of Calgary, April 2004

[33] Allans Time " http://www.allanstime.com/AllanVariance/index.html" (Accessed 19 August,2009)

[34] IMAR iTES-PDT07 Rate Table Operator's Manual, Imar Navigation, April 2007

[35] MicroStrain 3DM-GX1 MEMS Inertial Measurement Unit - MicroStrain Microminiature Sensors, http://www.microstrain.com/3dm-gx1.aspx (Accessed 19 August,2009)

[36] Stockwell W., *Bias Stability Measurement:Allan Variance*, Crossbow Technology Inc. http://www.xbow.com/support/Support_pdf_files/Bias_Stability_Measurement.pdf ,(Accessed 19 August 2009)

[37] Boasman N. et al , "Advanced Test Methods for Integrated Navigation Systems", *Royal Institute of Navigation*, 2005

[38] Sayed ZF et al., "A new multi-position calibration method for MEMS inertial navigation systems", *Measurement Science and Technology*, 2007

[39] Bar-Shalom Y., Li X.R., Kirubarajan T., *Estimation with Applications to Tracking and Navigation*, John Wiley and Sons, 2001

[40] Aydın Alatan Robot Vision Lecture Notes, Middle East Technical University, 2007

[41] Maybeck P.S., *Stochastic Models Estimation and Contol,* Academic Press Inc., 1979

[42] You S., Neumann U., "Fusion of Vision and Gyro Tracking for Robust Augmented Reality Registiration", *IEEE Virtual Reality Conference,* 2001

[43] You S., Neumann U., Azuma R., "Hybrid Inertial and Vision Tracking for Augmented Reality Registiration", *IEEE Virtual Reality Conference,* 1999

[44] Strelow S., Singh S., "Online Motion Estimation from Image and Inertial Measurements", *Workshop on Integration of Vision and Inertial Sensors INERVIS,* June 2003

[45] Cascaded Position-Velocity Loops, Danaher Motion Technical Note, 2000

[46] Ogata K., *Modern Control Engineering*, Prentice Hall, 1997

[47] *NIST/SEMATECH e-Handbook of Statistical Methods*, http://www.itl.nist.gov/div898/handbook/, (Accessed 22 August 2009)

[48] Grewall M.S., Andrews A.P., *Kalman Filtering: Theory and Practice Using Matlab,* Wiley and Sons Inc.,2001

[49] Aykın M.D., "Efficient Calibration of a Multi-Camera Measurement System Using a Target With Known Dynamics", Ms. Thesis, Middle East Technical University, August 2008

[50] Welch G., Bishop G., "An Introduction to the Kalman Filter", *Special Interest Group on Graphics and Interactive Techniques Conference*, 2001

[51] Huster A., Rock S.M., "Relative Position Sensing by Fusing Monocular Vision and Inertial Rate Sensors", *International Conference on Advanced Robotics,* 2003

[52] Nebot E., Durrant-Whyte H., "Initial Calibration and Alignment of Low-Cost Inertial Navigation Units for Land Vehicle Applications", Journal of Robotic Systems, Vol.16 Is.2 , 1999

[53] Dissanayake G. et al., "The Aiding of a Low-Cost Strapdown Inertial Measurement Unit Using Vehicle Model Constraints for Land Vehicle Applications", *IEEE Transactions on Robotics and Automation,*Vol.17 No.5, October 2001.